Chinese Journal of Chemical Engineering 95 (2026) 23–40

Contents lists available at ScienceDirect

Chinese Journal of Chemical Engineering

journal homepage: www.elsevier.com/locate/CJChE

Full Length Article

Numerical investigation of microporous layer structure on mass transport and durability in proton exchange membrane water electrolyzers

Lei Zhang [1, 2], Youliang Cheng [2, *], Yipeng Zhang [1], Chen Ju [1], Tianrang Yang [1]

[1] Beijing Laboratory of New Energy Storage Technology, Institute of Energy Power Innovation, North China Electric Power University, Beijing 102206, China
[2] Key Laboratory of Energy Storage and Integrated Energy Systems North China Electric Power University, Baoding 071003, China

ARTICLE INFO

Article history:
Received 27 October 2025
Received in revised form
2 February 2026
Accepted 10 February 2026
Available online 10 March 2026

Keywords:
Proton exchange membrane water electrolyzer
Microporous layer
Hydrogen safety
Numerical simulation

ABSTRACT

Proton exchange membrane water electrolyzers (PEMWEs) are considered a core technology for high-purity hydrogen production and renewable energy integration. Their performance and durability are strongly governed by electrode microstructural design. To address systematic studies on the role of the microporous layer (MPL) in electrolyzers gap, we develop a two-dimensional, two-phase, multiphysics-coupled model to investigate how MPL location, thickness, porosity, and wettability affect electrolysis performance, oxygen distribution, and the pressure difference across the membrane. The results show that the effect of the anode MPL is significantly stronger than that of the cathode, effectively improving oxygen distribution uniformity by 16.3%, reducing liquid water saturation at the anode, and optimizing gas–liquid co-transport. Increasing the MPL thickness markedly enhances the oxygen mole fraction in the catalyst layer and improves distribution uniformity; however, excessive thickness or extreme hydrophobicity/hydrophilicity leads to performance deterioration. More importantly, the presence of the anode MPL reduces the transmembrane gas pressure difference by up to 50%. In addition, the thickness, porosity, and hydrophobicity synergistic optimization can improve efficiency while enhancing safety and durability at high current densities. The optimal AMPL parameters are proposed as the thickness of 50–90 μm, contact angle of 80°, and porosity of 0.2–0.3. This study provides theoretical insights and practical guidance for electrode microstructural design in PEMWEs, with important implications for large-scale applications.
© 2026 The Chemical Industry and Engineering Society of China, and Chemical Industry Press Co., Ltd. All rights are reserved, including those for text and data mining, AI training, and similar technologies.

1. Introduction

Proton exchange membrane water electrolyzers (PEMWEs) are widely recognized as a cornerstone of future green hydrogen production, owing to their high-purity hydrogen output, rapid dynamic response, and compatibility with renewable energy. Nevertheless, they still face persistent challenges at high current densities, including mass-transport limitations, high noble-metal loading, and durability concerns, rendering electrode structural design particularly critical. Among electrode components, the microporous layer (MPL) has been extensively studied in fuel cells for its role in facilitating mass transport and water management, whereas its functions in electrolyzers have been less systematically explored. Recent studies indicate that MPLs can mitigate hydrogen crossover, enhance interfacial reaction activity, and improve durability. Thus, a deeper mechanistic understanding and design optimization of MPLs in PEMWEs are urgently needed to guide the development of efficient, cost-effective, and long-lasting electrolyzers.

In terms of thickness Sakaida *et al.* demonstrated that reducing MPL thickness can significantly lower mass-transport resistance at high current densities, thereby enhancing the peak power density of fuel cells [1]. Zhang *et al.* found that mechanical compression markedly decreases porosity and permeability, which intensifies local transport resistance [2]. Further investigations revealed that compression-induced interfacial deformation leads to non-uniform local water distribution and increased oxygen transport resistance [3]. According to Tayarani-Yoosefabadi *et al.*, the stochastic nature of microporous structures exerts a pronounced effect on overall transport uniformity and cell performance [4]. Nishimura *et al.* examined the impact of MPL thickness on temperature distribution, showing that the presence of an MPL can

* Corresponding author.
E-mail address: ylcheng@ncepu.edu.cn (Y. Cheng).

https://doi.org/10.1016/j.cjche.2026.02.003
1004-9541/© 2026 The Chemical Industry and Engineering Society of China, and Chemical Industry Press Co., Ltd. All rights are reserved, including those for text and data mining, AI training, and similar technologies.

mitigate localized overheating under high-temperature conditions. However, excessive thickness may raise thermal resistance and impair heat-transfer performance [5,6].

Analyze from the perspective of pores. García-Salaberri and Sánchez-Ramos systematically analyzed, through numerical simulations, the influence of microstructural parameters in the membrane electrode assembly on mass transport and reaction distribution under two-phase conditions. Their results indicated that larger pore structures in the MPL help alleviate local liquid water accumulation and reduce transport resistance, whereas excessively small pore sizes hinder gas transport, leading to reaction non-uniformity [7]. Chen *et al.* employed X-ray tomography to quantitatively characterize the porosity and its spatial distribution in the MPL, revealing that pore non-uniformity significantly affects local gas permeability and water removal characteristics [8]. Lan *et al.* found that cracks in the MPL induce localized reaction non-uniformity, thereby deteriorating overall fuel cell performance [9]. Jiang *et al.* demonstrated that rational perforation of the MPL facilitates liquid water removal, reduces flooding risks, and consequently enhances power density [10]. Wu *et al.* achieved highly engineered pore structures in the MPL through precise microstructural control, showing that such designs markedly improve oxygen transport efficiency and power output [11]. Song constructed carbon network structures within the MPL, which enhanced gas diffusion and mitigated liquid water retention [12]. Liu *et al.*, combining experiments and modeling, systematically investigated the roles of pore size and porosity in water transport, concluding that smaller pores help retain water but aggravate gas transport resistance, whereas larger pores favor gas diffusion [13]. However, the above analysis is mostly based on fuel cell, and porosity may have different effects on electrolyzers.

Hydrophilicity also plays an important role. Mohseninia *et al.* modified the MPL and catalyst layer (CL) structure, showing that macroporous designs redistribute two-phase flow, improve mass transport under both humidified and dry conditions, and enhance high-current performance [14]. Li *et al.* fabricated electrospun MPLs with distinct hydrophilic and hydrophobic properties and demonstrated that hydrophobic MPLs perform better under humid conditions, whereas hydrophilic MPLs are advantageous in dry environments, highlighting the strong coupling between thickness and wettability [15]. Building on this, Lin *et al.* reported that bilayer MPLs with matched thickness and hydrophobicity mitigate water retention and enhance gas transport efficiency, a finding later confirmed experimentally by Lin *et al.* [16,17]. Zhang *et al.* developed a superhydrophobic MPL by silane modification of carbon black, increasing the contact angle from 63° to 157°, which significantly improved gas permeability, water discharge, and single-cell power density [18]. Wang *et al.* designed hydrophobic/hydrophilic composites that maintained stable transport and performance under varying humidity [19], while Ira *et al.* incorporated dual hydrophilic–hydrophobic layers, combining simulations and experiments to demonstrate improved water-pathway distribution and reduced cathode water retention [20]. Wu *et al.* further underscored the dual role of MPLs in structural integrity and mass transport, highlighting their potential in both fuel cells and electrolyzers [21].

Despite the significant progress achieved in fuel cells, systematic investigations of MPLs in PEMWEs remain scarce, with most studies restricted to preliminary experimental exploration. Nevertheless, MPLs fulfill pivotal roles in electrolyzers by enhancing performance, reducing hydrogen crossover, and improving electrode–electrolyte interfacial properties. Recent research has therefore increasingly centered on their structural design, functional optimization, and fabrication methods [22]. Ding *et al.* modified anode-side MPLs and demonstrated enhanced interfacial activity, which led to higher hydrogen yield and efficiency [23]. Wang *et al.* proposed bifunctional cathode MPLs that simultaneously suppressed hydrogen crossover and improved electrochemical performance, thereby offering a strategy to balance safety and efficiency [24]. Ernst and Zou *et al.* systematically fabricated and characterized MPL-based transport layers, demonstrating that their microstructures govern two-phase water/gas transport and thus electrolyzer stability and performance [25,26]. Schuler *et al.* designed ultrathin MPLs, which, under low Ir loadings, thin membranes, and high current densities, reduced ohmic resistance and broadened the safe operating window [27]. Zou *et al.* constructed gradient-structured gas diffusion layers by incorporating Nafion resin with different mass fractions into the MPL, thereby improving water management on the anode side [28,29]. Kulkarni *et al.* demonstrated that MPLs improve oxygen distribution and significantly extend durability in PEMWEs [30]. Zeng *et al.* conducted numerical evaluations of MPL-integrated PEMWEs, confirming that MPLs critically optimize electrode coupling and overall efficiency [31].

Overall, the structure of the MPL governs two-phase transport, local reaction activity, and overall performance in PEM fuel cells. At the present stage, the roles of MPLs in PEM water electrolyzers are mainly associated with suppressing hydrogen crossover and enhancing long-term durability. However, how specific MPL structural and interfacial characteristics influence transport processes, electrochemical behavior, and operational performance in PEMWEs, as well as the extent and mechanisms of these impacts, remain insufficiently understood and warrant systematic investigation. In view of this, this work develops a two-dimensional, two-phase, multiphysics-coupled electrolyzer model based on the agglomerate framework. The model is applied to examine the effects of MPL location, thickness, porosity, and contact angle on PEMWE operation, aiming to elucidate underlying mechanisms and optimization pathways. The findings offer both theoretical insights and practical guidance for the development of efficient, safe, and durable green hydrogen technologies.

2. Modeling and Methods

2.1. Model introduction

The geometric model employed in this study represents a two-dimensional single-channel electrolyzer unit, comprising flow channels (CH), porous transport layers (PTL), anode and cathode catalyst layers, and a proton exchange membrane (PEM). At the anode, the inlet is supplied with a mixture of liquid water, water vapor, and oxygen, with the outlet defined in the same manner. Likewise, the cathode inlet receives a mixture of liquid water, water vapor, and hydrogen, and its outlet is also specified as a gas–liquid mixture. Each computational domain incorporates the relevant physical processes, as illustrated in Fig. 1. To reflect realistic PEMWE operating conditions, the model is established under the following assumptions:

(1) The internal flow within the electrolyzer is laminar;
(2) The system operates under steady-state conditions;
(3) All gases are considered ideal gases.

The geometric parameters adopted in this study are presented in Table 1, and the parameters of the agglomerate model are shown in Table 2.

The thicknesses of the anode catalyst layer (ACL) and cathode catalyst layer (CCL) are linearly correlated with the catalyst loading [32], as shown in Fig. 2(a) and (b) represents the transmission

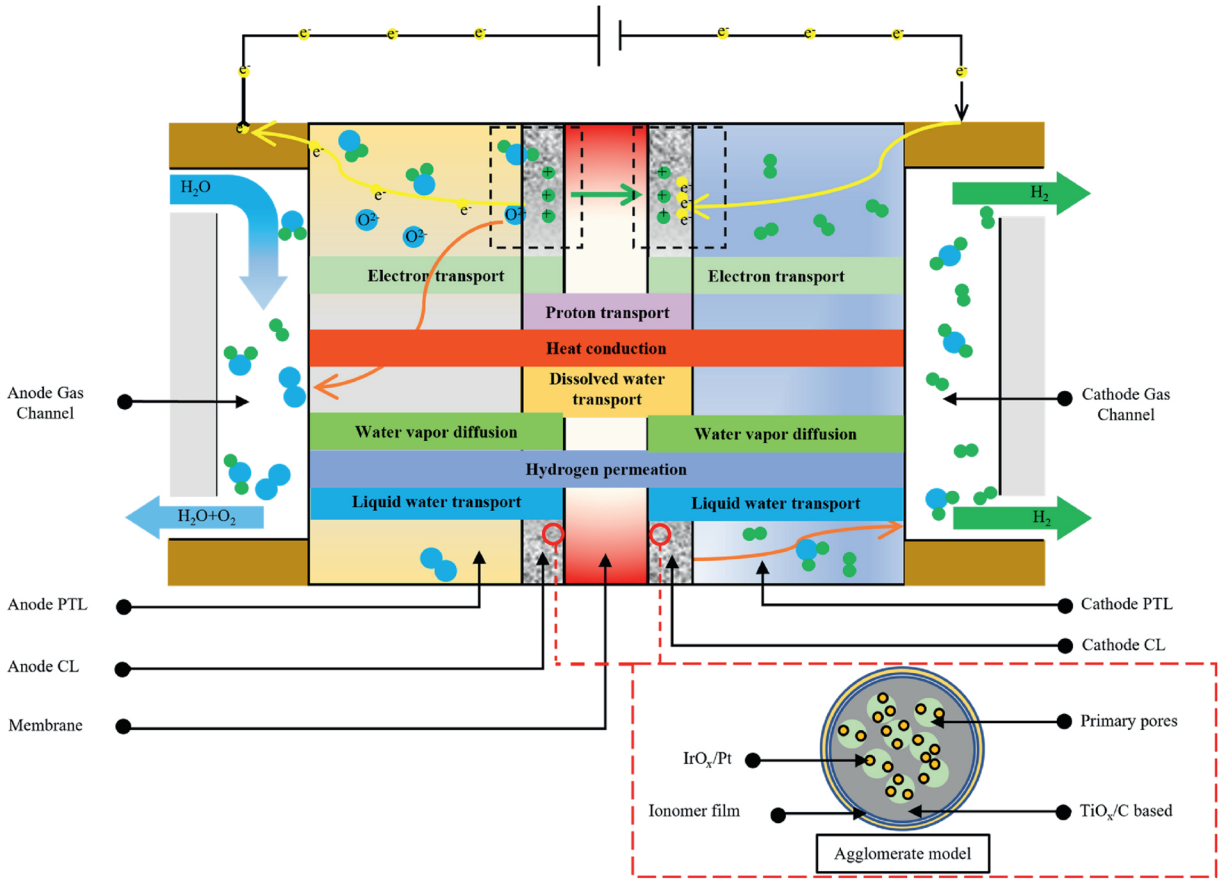


Fig. 1. The computational domain of PEMWE.

Table 1
Parameters of geometry.

Parameter	Value	Unit
Thickness of PEM (Nafion N115/N117)	127, 178	μm
Thickness of PTL	0.25/0.25	mm
Channel depth	1	mm
Width of channel	1	mm
Channel length	50	mm

Table 2
Agglomerate model parameters.

Parameter, unit	Equation/value
Reference exchange current density, $A \cdot m^{-3}$	$i_a^{ref} = 0.0025\ i_c^{ref} = 10000$
Reference reactant concentration [41], $mol \cdot m^{-3}$	$C_{H_2}^{ref} = 56.4, C_{O_2}^{ref} = 3.39$
Transfer coefficient	$\alpha_a = 0.5, \alpha_c = 0.5$
Henry's constant [44], $Pa \cdot m^3 \cdot mol^{-1}$	$H_{H_2} = 4560, H_{O_2} = 0.101325\exp\left(-\frac{666}{T} + 14.1\right)$
Density of Ir/Pt [33], $kg \cdot m^{-3}$	$\rho_{Ir} = 22500, \rho_{Pt} = 21450$
Carbon density [45], $kg \cdot m^{-3}$	$\rho_C = 1800$
Ir/Ti and Pt/C mass ratio	$f = 0.75/0.6$
Membrane swelling coefficient [34]	$k_s = 0.0126$
Ir/Pt loading, $mg \cdot cm^{-2}$	$m_{Ir,a} = 1.5\ m_{Pt,c} = 0.1$
Ionomer content [46]	$\varepsilon_i = 0.29$
Agglomerate radius [38], m	$r_{agg} = 6.1 \times 10^{-7}$
Electrolyte content within agglomerates [38]	$\varepsilon_{i,agg} = 0.31$

electron microscope (TEM) of ACL and CCL, and their morphology is consistent with that described by the agglomerate model.

2.2. Agglomerate model

The catalyst layer domain in the electrolyzer was modeled using the agglomerate model, where the finite-thickness medium consists of catalyst particles, ionomer, and pores, with the ionomer assumed to swell under fully hydrated conditions [33,34]:

$$\varepsilon_{CL} + \varepsilon_s + (1 + k_s\lambda)\varepsilon_i = 1 \tag{1}$$

here, ε_{CL} denotes the porosity of the catalyst layer, ε_s is the volume fraction of catalyst particles (Ir for the anode and Pt for the cathode), ε_i represents the ionomer volume fraction, k_s is the swelling coefficient, and λ denotes the water content.

The catalyst particle volume fraction is related to the catalyst loading, the densities of the metal and support, and their mass ratio [35]:

$$\varepsilon_s = \frac{m_{IrO_x/Pt}}{H_{ACL/CCL}}\left(\frac{1}{\rho_{Ir/Pt}} + \frac{1-f}{f}\frac{1}{\rho_{TiO2/C}}\right) \tag{2}$$

here, $m_{IrO_x/Pt}$ denotes the catalyst loading, corresponding to IrO_x in the anode catalyst layer and Pt in the cathode catalyst layer. $H_{ACL/CCL}$ represents the thickness of the anode and cathode catalyst layers.

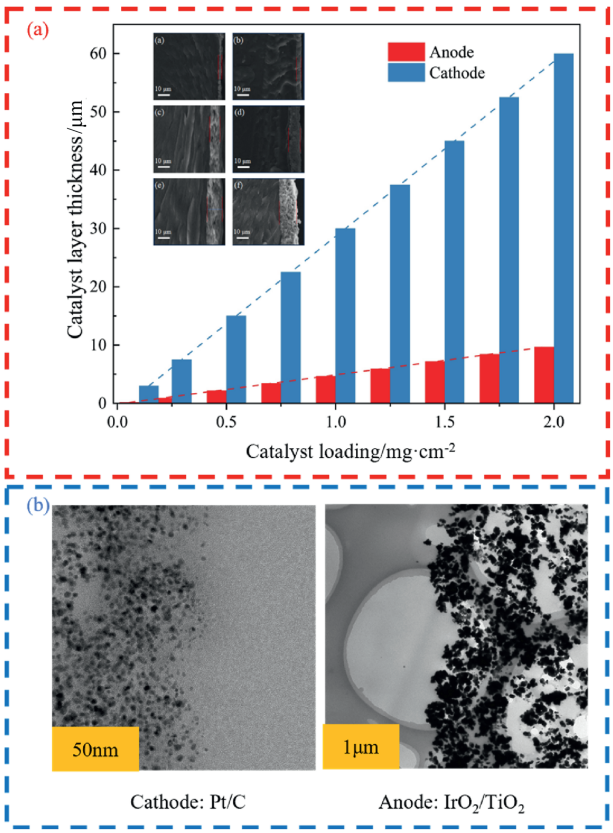


Fig. 2. (a) Relationship between catalyst loading and CL thickness, (b) TEM of ACL and CCL.

$\rho_{Ir/Pt}$ is the catalyst density (IrO_x for the anode and Pt for the cathode). $\rho_{TiO2/C}$ denotes the support density, with TiO_2 for the anode and carbon for the cathode. Finally, f represents the mass ratio of IrO_x to Ti in the anode, and of Pt to C in the cathode [36]:

$$f = \frac{m_{IrO_x/Pt}}{m_{IrO_x/Pt} + m_{TiO2/C}} \tag{3}$$

Assuming that the agglomerates are uniformly distributed within the catalyst layer, the number of agglomerates per unit volume can be calculated as follows [37]:

$$N_{agg} = \frac{\varepsilon_s}{4\pi/3 r_{agg}^3 \left(1 - \varepsilon_{i,agg}\right)} \tag{4}$$

here, r_{agg} denotes the agglomerate radius; $\varepsilon_{i,agg}$ is the volume fraction of ionomer within the agglomerate; and ε_s represents the volume fraction of catalyst particles.

An agglomerate is composed of catalyst particles supported with noble metals, and it is surrounded by an ionomer film, whose thickness δ_i can be calculated as follows [38]:

$$\delta_i = r_{agg}\left(\sqrt[3]{\frac{\varepsilon_i\left(1 - w_{i,a}\right)}{\varepsilon_s} - \varepsilon_{i,agg} + 1} - 1\right) \tag{5}$$

After being generated on the catalyst surface, oxygen diffuses through the ionomer film. If oxygen removal is hindered, the reaction rate decreases; therefore, an effectiveness factor E_r is defined. Physically, it represents the ratio of the actual reaction rate to the expected rate under the ideal condition where all catalyst particles are exposed on the support surface without any loss of active sites [39].

$$E_r = \frac{1}{\phi}\left(\frac{1}{\tanh(3\phi)} - \frac{1}{3\phi}\right) \tag{6}$$

here, ϕ denotes the Thiele modulus of the chemical reaction, which represents the amount of reaction occurring on the external surface per unit mass of catalyst per unit time at a given temperature, characterizing the influence of oxygen diffusion within the agglomerate on the overall reaction [39]:

$$\phi = \frac{r_{agg}}{3}\sqrt{\frac{k_c}{\varepsilon_{i,agg}^{1.5} D_{O_2,i}}} \tag{7}$$

here, $D_{O_2,i}$ is the diffusion coefficient of oxygen in the ionomer, and k_c is the reaction rate constant [39]:

$$k_c = \frac{i_a^{ref} A_{eff}}{4F(1 - \varepsilon_{CL}) C_{O_2}^{ref}}\left(e^{2\alpha_a F\eta_a/R/T} - e^{-2\alpha_a F\eta_a/R/T}\right) \tag{8}$$

here, i_a^{ref}, A_{eff}, $C_{O_2}^{ref}$, and α_a represent the anode reference exchange current density, the effective specific surface area of the catalyst, the reference oxygen concentration, and the anode transfer coefficient, respectively [40].

$$A_{eff} = \frac{(1 - \varepsilon_{CL}) m_{IrO_x/Pt}}{\varepsilon_i H_{ACL/CCL}} A_0 \tag{9}$$

here, A_0 denotes the specific surface area per unit mass of catalyst, corresponding to Ir at the anode and Pt at the cathode [40]:

$$A_0 = \left(227.79 f^3 - 158.57 f^2 - 201.53 f + 159.5\right) \times 10^3 \tag{10}$$

η_a is the anode overpotential, expressed as:

$$\eta_a = \phi_{ele} - \phi_{ion} - E_{eq} \tag{11}$$

here, E_{eq} denotes the equilibrium potential [41]:

$$E_{eq} = 1.229 - 0.9 \times 10^{-3}(T - 298.15) \tag{12}$$

The electronic and ionic potentials are calculated using electrochemical conservation equations:

$$0 = \nabla\cdot\left(\sigma_{ele}^{eff}\nabla\phi_{ele}\right) + S_{ele} \tag{13}$$

$$0 = \nabla\cdot\left(\sigma_{ion}^{eff}\nabla\phi_{ion}\right) + S_{ion} \tag{14}$$

here, S_{ele} and S_{ion} denote the source terms of electronic and ionic conservation, respectively.

In the agglomerate model, agglomerates are interconnected to conduct ions. Variations in ionomer film thickness alter the proton conductivity within the catalyst layer: when the ionomer film becomes thinner, the connectivity between agglomerates decreases accordingly. Considering the contact area between agglomerates, the effective proton conductivity of the catalyst layer can be estimated using the following equation [42]:

$$\sigma_{ion}^{eff} = (1 - \varepsilon_{CL})\left[1 + \frac{\left(\varepsilon_{i,agg} - 1\right)}{\left(1 + \delta_i/r_{agg} + a_0\right)^3}\right]\sigma_{ion} \tag{15}$$

$$a_0 = min\left[0, \left(\frac{\delta_i}{r_{agg}} + \left(1 - \varepsilon_{i,agg}\right)^{\frac{1}{3}} - 1\right)\right] \tag{16}$$

here, a_0 is an auxiliary parameter introduced to ensure that the proton conductivity approaches zero as the ionomer film thickness tends to zero. σ_{ion} denotes the ionic conductivity, which depends on temperature T and membrane water content λ [35].

$$\sigma_{ion} = (0.5139\lambda - 0.326)\exp\left[1268\left(\frac{1}{303} - \frac{1}{T}\right)\right] \tag{17}$$

The effective electronic conductivity in the catalyst layer is corrected using the following equation:

$$\sigma_{ele}^{eff} = \varepsilon_s^{1.5}\sigma_{ele} \tag{18}$$

The electrochemical reaction kinetics are calculated using the Butler–Volmer equation. In the CL, the equation is modified with agglomerate model parameters to account for the influence of agglomerate characteristics on transport resistance. Within the agglomerate model, the volumetric reaction rate of the oxygen evolution reaction (OER) in the ACL is expressed as follows [33]:

$$J_a = 4F\left(\frac{P_{O_2}}{H_{O_2}}\right)\left(\frac{1}{E_r k_c} + \frac{(r_{agg} + \delta_i)\delta_i}{r_{agg} a_{agg,i} D_{O_2,i}}\right)^{-1} \tag{19}$$

here, $a_{agg,i}$ and $a_{agg,w}$ denote the effective surface areas in the electrolyte and in water within the agglomerate, respectively, while the fractional term represents the agglomerate resistance:

$$a_{agg,i} = \frac{3\varepsilon_S\varepsilon_{CL}}{r_{agg}^3\left(1 - \varepsilon_{i,agg}\right)}(\delta_i + r_{agg})^2 \tag{20}$$

The volumetric reaction rate of the hydrogen evolution reaction (HER) in the CCL is expressed as [43]:

$$J_c = (1 - s)i_c^{ref}A_{eff}\left(\frac{P_{H_2}}{C_{H_2}^{ref}H_{H_2}}\right)^{0.5}\left(e^{-2\alpha_c F\eta_c/R/T} - e^{2\alpha_c F\eta_c/R/T}\right) \tag{21}$$

here, s, i_c^{ref}, P_{H_2}, H_{H_2}, $C_{H_2}^{ref}$ and α_c denote the liquid water saturation, cathode reference exchange current density, hydrogen partial pressure, Henry's constant for hydrogen, reference hydrogen concentration, and cathode transfer coefficient, respectively. η_c and A_{eff} represent the cathode overpotential and the effective reactive surface area, respectively. The liquid water saturation is solved within the two-phase flow model.

The cathode overpotential is expressed as:

$$\eta_c = \phi_{ele} - \phi_{ion} \tag{22}$$

2.3. Establish the numerical model

The total normal current density is applied at boundary B–b, while boundary G–g is set as a zero-potential boundary. The temperature at both boundaries is fixed at an isothermal condition of 353.15 K. The anode and cathode inlets are specified as velocity inlets, while the anode and cathode outlets are defined as pressure outlets with ambient pressure. The liquid water saturation at both inlets is set to 90%, and the inlet water temperature is 353.15 K. As shown in Fig. 3(a) and Table 3.

The modeling, meshing, and simulations were carried out using the commercial finite element software COMSOL Multiphysics 6.3. The electrolyzer module was employed to solve the electrochemical and gas species equations; Darcy's law was used to compute the liquid water pressure in the anode and cathode; the multiphase transport in porous media interface was used to determine liquid water saturation; heat transfer was modeled using both solid and fluid heat transfer modules; and membrane water transport was simulated using the dilute species transport interface to capture water adsorption/desorption and membrane water content. Parametric sweeps were performed under various structural and operating conditions, including layer thicknesses, inlet liquid water temperature, inlet liquid water velocity, and different CL or PTL parameters such as porosity, ionomer volume fraction, agglomerate radius, and contact angle, within a current density range of 0.1–3 A·cm^{-2} to obtain the polarization curves of the PEMWE. All simulations were conducted on a workstation equipped with an Intel Core™ i7-13700K CPU (3.40 GHz, Turbo up to 5.4 GHz) and 32 GB of RAM.

As shown in Fig. 3(b), a detailed grid independence verification was conducted in both the *X* and *Y* directions. For the *X*-direction test, the number of grid nodes was set to 100. For the *Y*-direction test, the number of grid nodes was fixed at 6 in the CH, PTL, and CL regions, and 8 in the MEM region, resulting in a very small error of less than 0.02%. In addition, all equations were solved under a convergence criterion of 10^{-4} to ensure computational accuracy.

$$\text{Error} = \frac{|I - I_{Nx=200}|}{I_{Nx=200}} \times 100\% \tag{23}$$

Since temperature couples with the electrochemical field, mass transfer field, flow field, and heat transfer field, changing the temperature will have a profound impact on the entire model, creating a strong bidirectional closed-loop coupling. Therefore, validating the model with three polarization curves at different temperatures can provide accurate predictive capability. Fig. 3(c) compares the experimental and simulation results. The experimental data were obtained by averaging at least three repeated measurements, yielding an average relative error of less than 0.5%. The simulation results are in good agreement with the experimental data.

In this study, the coefficient of variation of variable *X* is employed to perform homogenization analysis. Where VCO represents oxygen distribution uniformity.

$$\text{VCX} = \sqrt{\frac{\sum (X_i - X_0)^2}{n - 1}} \Big/ X_0 \tag{24}$$

A membrane area of 2.5 cm × 2.5 cm was used in this study, as shown in Fig. 4. Catalyst ink was sprayed using an XF400 sprayer (China). For the hydrogen evolution reaction (HER) and oxygen evolution reaction (OER), Pt/C (60% (mass) Pt on Vulcan XC72, TEC10E60TPM; Tanaka Kikinzoku Kogyo, Japan) and IrO_x (75% (mass) Ir on TiO_2, Elyst Ir75 0480; Umicore, Germany) catalysts were used, respectively. A Nafion N115 proton exchange membrane with a thickness of 127 μm was employed. The anode porous transport layer (PTL) was titanium felt from Bekaert (Belgium), while the cathode PTL was H2C483 carbon paper from Freudenberg (Germany). The membrane electrode assembly (MEA) was fabricated by hot pressing at 140 °C and 4410 N for 3 min to form a five-in-one structure. The assembly sequence followed the layout shown in the diagram: anode end plate, heating plate, insulating cloth, flow field plate, PTFE layer, and MEA, followed by a symmetric arrangement on the cathode side. Bolts and nuts were tightened to complete the electrolyzer assembly. The tubing was then connected. The anode outlet was connected to a gas–liquid separator. The liquid stream was re-purified through an

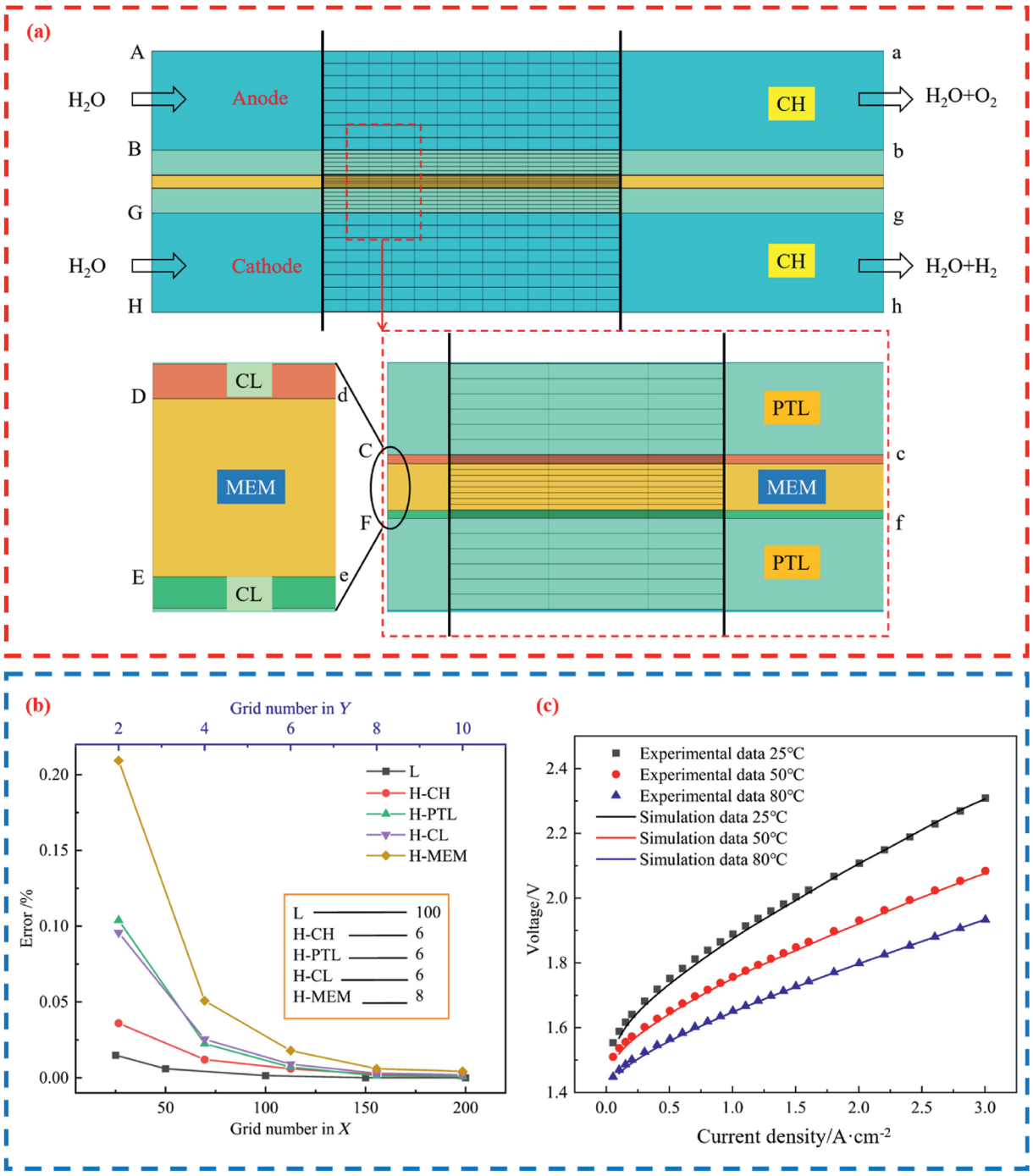


Fig. 3. (a) Boundaries and mesh of the 2D electrolyzer model. (b) Grid Independence Verification. (c) Polarization curves from simulation and experiment.

Table 3
Boundary conditions.

Boundaries	Expressions
Boundary B-b	I
Boundary G-g	Electrical grounding: $\phi_{ele} = 0$
Liquid water inlet velocity A-B, G-H	$u_a = u_c = u_{in} = 0.3333\ m \cdot s^{-1}$
Outlet pressure a-b, g-h	$P_{a,out} = P_{c,out} = 1$ atm
Liquid water saturation conservation A-B, G-H	$s_a = 0.9 \quad s_c = 0.9$
Boundaries A-B, G-H	$T_a = T_c = T_{in} = 353.15$ K

ultrapure resin column (IA-SCH-45, China) before reentering the anode inlet. Airflow is expelled upwards. A customized test station equipped with a DC power supply (16 V/250 A/1.8 kW, model N3618-016-250, NGI, China) was used to conduct the experiments. To investigate hydrogen leakage, all connections were carefully inspected to eliminate unintended leaks. The electrolyzer's I–V polarization curve was recorded using the same test station. During activation, 80 °C deionized water was supplied to the anode using a peristaltic pump, and the activation process lasted for 8 h. Afterward, the electrolysis voltage was set to 1.6 V, and the

Table 4
Properties of different MPLs.

Parameter	Anode	Cathode	Thickness/μm	Porosity	Contact angle/(°)
Case 1	×	×	/	/	/
Case 2	○	×	10,30,50,90,110	0.1,0.2,0.3,0.4,0.5,0.6	20,50,80,100,130,160
Case 3	×	○	10,30,50,90,110	0.1,0.2,0.3,0.4,0.5,0.6	20,50,80,100,130,160
Case 4	○	○	10,30,50,90,110	0.1,0.2,0.3,0.4,0.5,0.6	20,50,80,100,130,160

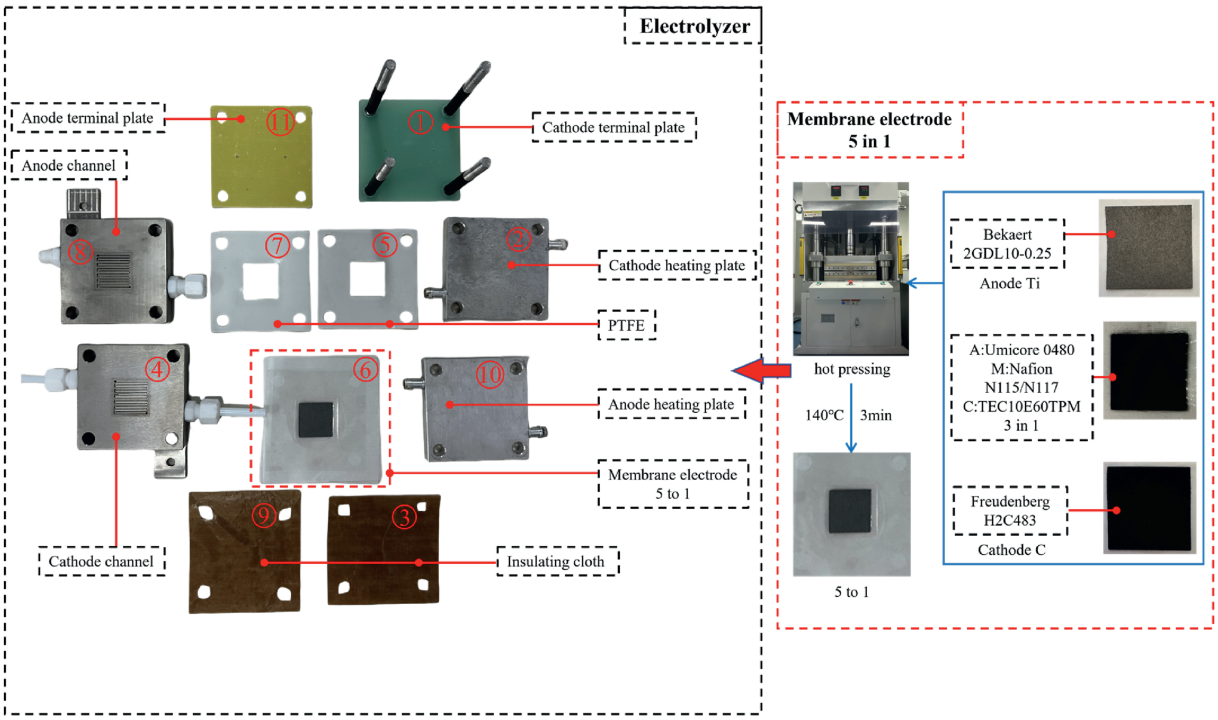


Fig. 4. Experimental design and measurement procedure.

operating current was monitored until a steady-state value was reached. Finally, polarization curves were obtained under galvanostatic conditions, with a step duration of 0.5 min.

3. Results and Discussion

3.1. Location of the MPL

As summarized in Table 4, the cases were defined based on the location of MPL addition: case 1 without MPLs at either electrode, case 2 with an MPL only at the anode, case 3 with an MPL only at the cathode, and case 4 with MPLs at both electrodes. Simulations were then conducted to evaluate the effects of MPL thickness, porosity, and contact angle. For all four cases with MPLs, the parameters were set as a thickness of 30 μm, a contact angle of 80°, and a porosity of 40%.

Fig. 5(a) shows the performance variations under four different cases. At a low current density of 0.5 $A \cdot cm^{-2}$, adding an AMPL improves performance by 11 mV, whereas a CMPL shows no noticeable effect. At a high current density of 3 $A \cdot cm^{-2}$, the presence of an AMPL adversely affects performance, causing a voltage drop of 15 mV. In contrast, a CMPL leads to a smaller drop of 5 mV. Moreover, when both AMPL and CMPL are present, their negative effects partially cancel each other out. This implies that introducing 30-μm-thick MPLs with 40% porosity on both electrodes exerts a weaker influence on performance than adding an MPL on only one side. Fig. 5(b) presents the Thiele modulus ϕ. When $\phi < 1$, the particle is fully utilized with uniform internal concentration, and reaction kinetics dominate the rate limitation. When $\phi > 1$, diffusion of water into the agglomerates becomes the dominant factor. Accordingly, when the current density exceeds 1.5 $A \cdot cm^{-2}$, the limitation shifts from kinetics to diffusion, and at higher current densities diffusion increasingly dominates the reaction. Fig. 5(c) shows the water content in the ACL, MEM, and CCL under various current densities. Initially, the water content in all three regions is close to 16. As the current density increases, the water content in the ACL decreases, reaching 11 at 3 $A \cdot cm^{-2}$. In the MEM, the water content first increases and then decreases with rising current density, while remaining above 15 in all cases. In the CCL, the electro-osmotic drag effect causes the water content to rise to above 27 at 3 $A \cdot cm^{-2}$. This leads to severe cathodic oversaturation. As shown in Fig. 5(d), moreover, introducing an AMPL shifts the onset of diffusion limitation to higher current densities. A significant improvement in oxygen distribution uniformity is observed only with the addition of an anode MPL. In this case, the overall VCO across the anode (ACH, APTL, and ACL) decreases by 16.3%, indicating a substantial enhancement in oxygen uniformity. Fig. 5(e) illustrates the effect of the MPL on the transmembrane gas pressure difference. The transmembrane gas pressure difference is defined as the gas pressure in CCL minus that in ACL. According to the electrolyzer reaction, the volume of hydrogen produced is twice that of oxygen.

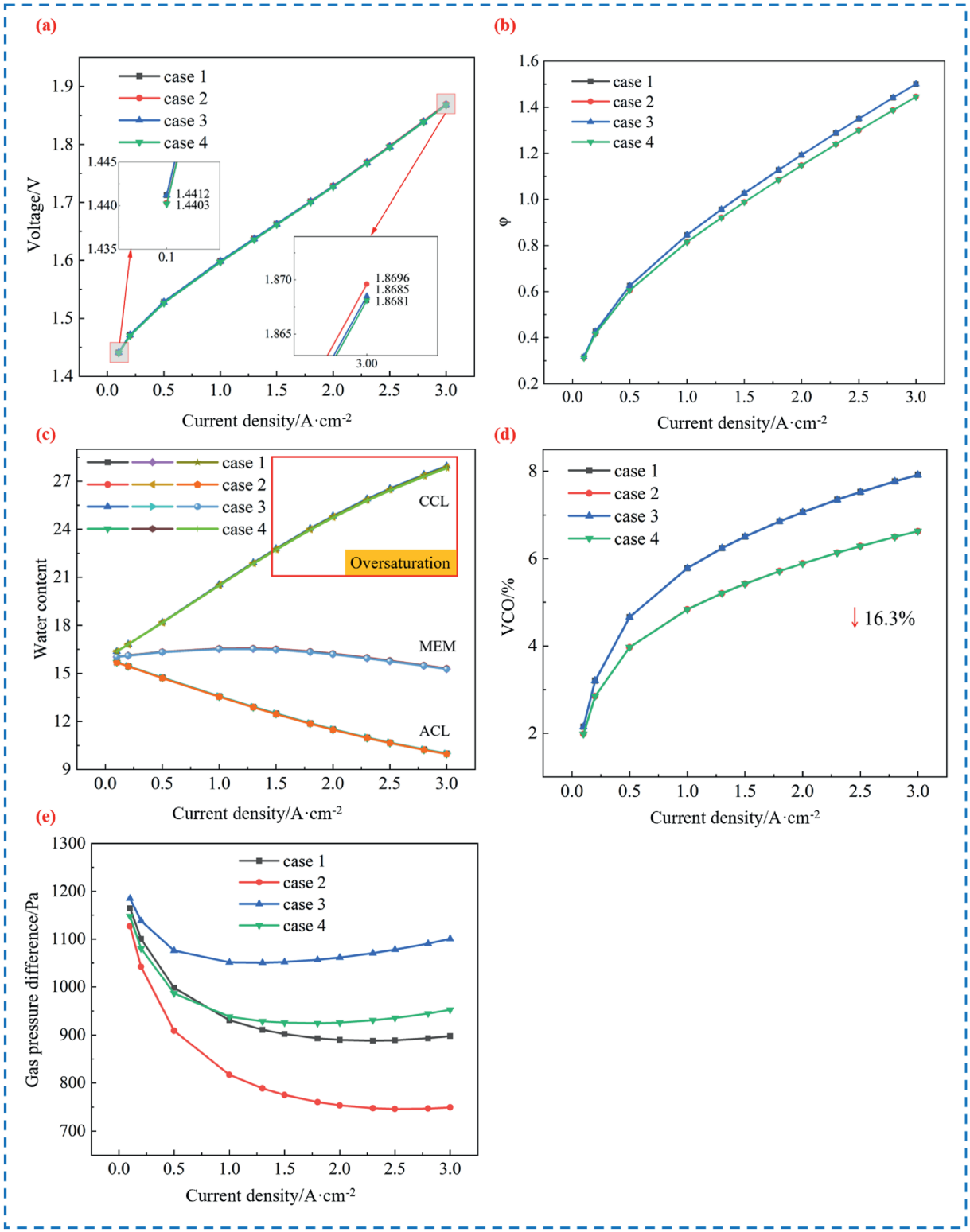


Fig. 5. (a) Polarization curves for the four cases, (b) Variation of Thiele modulus, (c) Water content in the membrane electrode under different current densities, (d) VCO, (e) Variation of transmembrane gas pressure difference.

Consequently, the gas pressure is generally higher on the cathode than on the anode during operation. In all cases, the pressure difference decreases initially and then increases as the current density rises. Introducing only a CMPL shifts the inflection point toward lower current densities, whereas an AMPL shifts it toward higher values. When both are present, the effect of the CMPL clearly dominates. In comparison, Case 1 and Case 4 show reductions of 22.9% and 17.02%, respectively. This behavior is mainly attributed to gas accumulation arising from the resistance of the MPL to oxygen at the anode and hydrogen at the cathode.

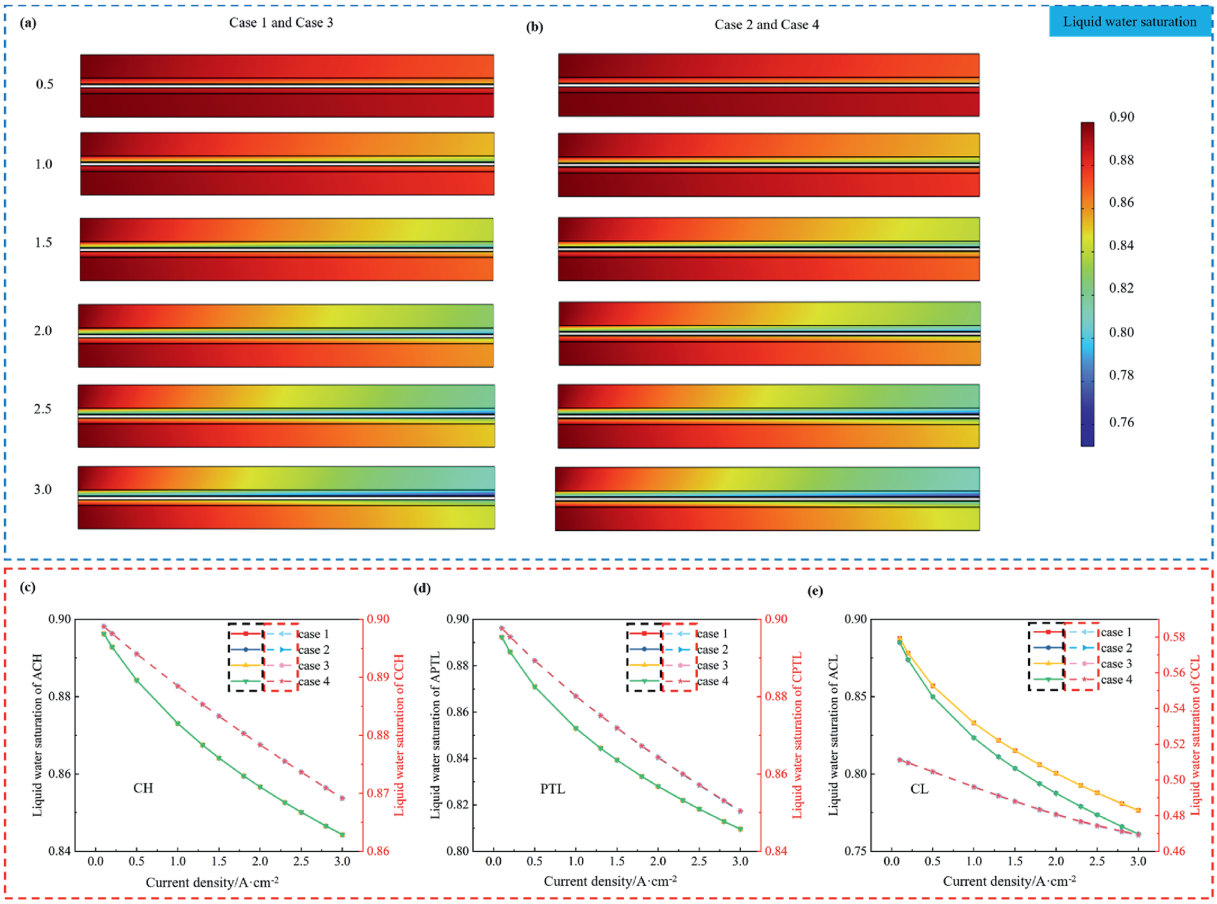


Fig. 6. Changes of liquid water saturation.

Fig. 6(a) and (b) show the variations in liquid water saturation across different regions of the anode and cathode under four cases at various current densities. The results indicate that at any current density, the saturation in the anode is consistently lower than that in the cathode, owing to water consumption in ACL during electrolysis. At the same current density, the influence of MPLs on saturation is negligible in other regions, except becomes significant in the ACL. In cases 2 and 4, the addition of an AMPL increases ACL saturation, and this effect intensifies at higher current densities, indicating that MPLs exert a stronger impact on the anode, where water concentration fluctuates more drastically. Refer to Fig. 6(c)–(e), for both the anode and cathode, the MPL has almost no influence on the liquid water saturation in the CL and the PTL. In contrast, the presence of the AMPL decreases the water retention capability of the ACL, thereby enhancing the decrease in liquid water saturation. In the ACL, the average saturation decreases from 0.8876 to 0.7765 (−12.52%) in cases 1 and 3, and from 0.8850 to 0.7611 (−14.01%) in cases 2 and 4. This phenomenon can be explained as follows: the addition of an AMPL increases the expulsion of oxygen generated within the ACL. The accumulated oxygen occupies the pore volume otherwise available to liquid water, thereby lowering the saturation. Consequently, by tuning AMPL properties, oxygen accumulation in the ACL can be effectively controlled, enabling improved performance and enhanced water–gas management in the electrolyzer.

Fig. 7 presents the variations in the mole fraction and partial pressure of oxygen and hydrogen, respectively. With only an anode MPL, according to Fig. 7(e) and (j), the oxygen partial pressure in the CL increases by 1888 Pa at a current density of 3 A·cm^{-2}. With only a cathode MPL, the hydrogen partial pressure in the CL increases by 2402 Pa at 3 A·cm^{-2}. In addition, the oxygen partial pressure decreases in the anode channel, whereas its variation in the APTL is negligible. The MPL has little effect on the hydrogen partial pressure in the cathode channel and cathode PTL. These results suggest that anode and cathode MPLs promote gas accumulation within the CL, thereby slightly increasing the local mole fraction.

The above results demonstrate that incorporating an MPL on the anode side is considerably more effective than on the cathode side. As a transition layer between the CL and PTL, the MPL optimizes water–gas transport by reducing liquid water saturation and increasing the oxygen mole fraction in the CL from 35.7% to 36.4%, thereby facilitating gas diffusion. The influence of MPLs is more pronounced at high current densities, as indicated by the more concentrated oxygen distribution in ACL and the slightly reduced oxygen partial pressure in the anode channel. This suggests that the AMPL helps retain a portion of oxygen in the ACL and improves overall distribution uniformity. Meanwhile, MPLs also play an important role in regulating the transmembrane gas pressure difference. An AMPL reduces the gas pressure in the ACL and lowers the transmembrane gas pressure difference, which may help decrease hydrogen crossover. By contrast, a CMPL increases the pressure difference, and when both MPLs are present, the overall pressure difference rises at high current densities.

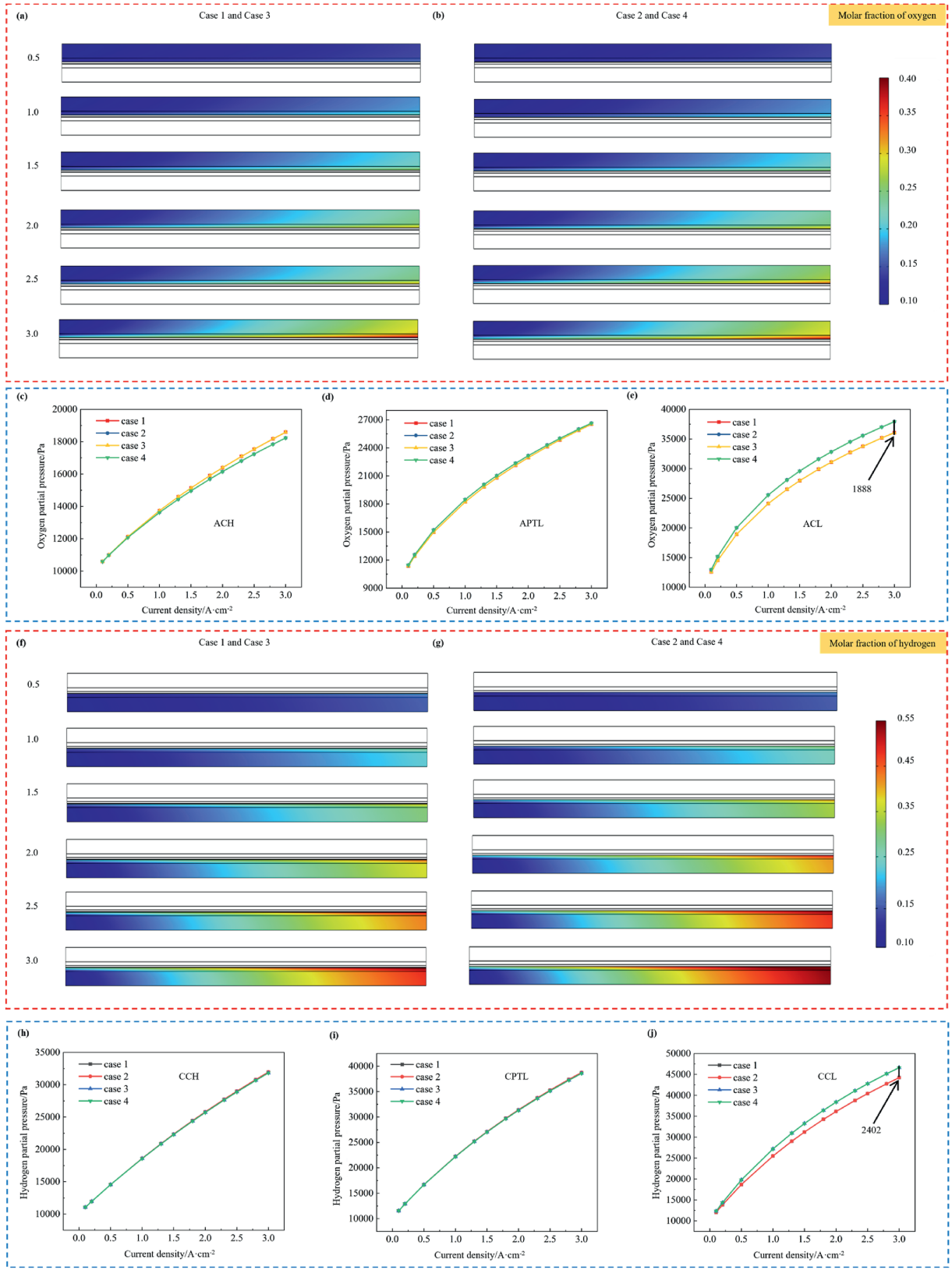


Fig. 7. Distribution of oxygen (a-e) and hydrogen (f-j) mole fraction and partial pressure.

In summary, the MPL not only enhances oxygen diffusivity but also reduces local gas pressure and mass-transfer resistance. These effects enable the electrolyzer to sustain a low pressure difference and a well-balanced gas–liquid distribution even at high current densities, thereby mitigating mass-transport polarization and improving both electrochemical performance and safety.

3.2. Impact of MPL's structural parameters on performance

Fig. 8(a) and (b) illustrate the influence of AMPL and CMPL thickness on cell performance. At 3 A·cm^{-2}, the performance difference between the thinnest and thickest AMPLs is 30 mV. Increasing the CMPL thickness from 10 to 110 μm improves performance by 33 mV at the same current density. Fig. 8(c) shows that a hydrophilic cathode MPL yields greater performance improvement than a hydrophobic one, with a maximum difference of 28 mV. However, excessive hydrophilicity or hydrophobicity results in performance degradation. The optimal performance occurs at a contact angle of 80°, whereas the poorest is observed at 100°. In contrast, the CMPL exerts only a minor influence of a few millivolts, far less than that of the AMPL. As the porosity increases from 0.1 to 0.6, cell performance gradually declines, with the voltage rising by approximately 10 mV at 3 A·cm^{-2}. Fig. 8(d) shows that at lower porosity, the AMPL generates stronger capillary forces, which facilitate oxygen removal and improve distribution uniformity, thereby enhancing overall performance.

3.3. Thickness of the MPL

As shown in Fig. 9(a) MPL thickness exerts little influence on liquid water saturation in the PTL and CH, but markedly affects that in the ACL. Increasing MPL thickness decreases liquid water saturation, thereby allowing gases to occupy a larger fraction of the pores. At 3 A·cm^{-2}, liquid water saturation decreases from 77.1% with a 10 μm MPL to 72.8% with a 110 μm MPL, corresponding to a 5.6% reduction. Meanwhile, the continuous rise in oxygen partial pressure reflects a higher oxygen fraction, indicating that oxygen progressively fills the pores vacated by displaced liquid water. Fig. 9(b) Illustrates the effect of CMPL thickness on the hydrogen partial pressure in CCL. An increase in cathode MPL thickness elevates the hydrogen partial pressure in the CL across different current densities, although the rise does not exceed 5000 Pa. By contrast, the hydrogen partial pressure exhibits little variation in the CPTL and CCH.

The effect of AMPL thickness on the Thiele modulus (φ), as Fig. 9(c), indicating that greater thickness shifts the current density at which diffusion becomes rate-limiting to higher values. This implies that a thicker AMPL delays the onset of oxygen diffusion restriction, requiring higher current densities before diffusion limits the reaction rate. Although an MPL lengthens the diffusion path from the CL to the channel and increases resistance, it simultaneously reduces φ, thereby alleviating diffusion limitations at a given current density. When φ approaches unity, the reaction and diffusion rates become comparable and balanced. In this regime, a thicker AMPL is more advantageous at high loads, shifting the relative optimum operating point toward higher current densities. The VCO with AMPL thickness at different current densities shows

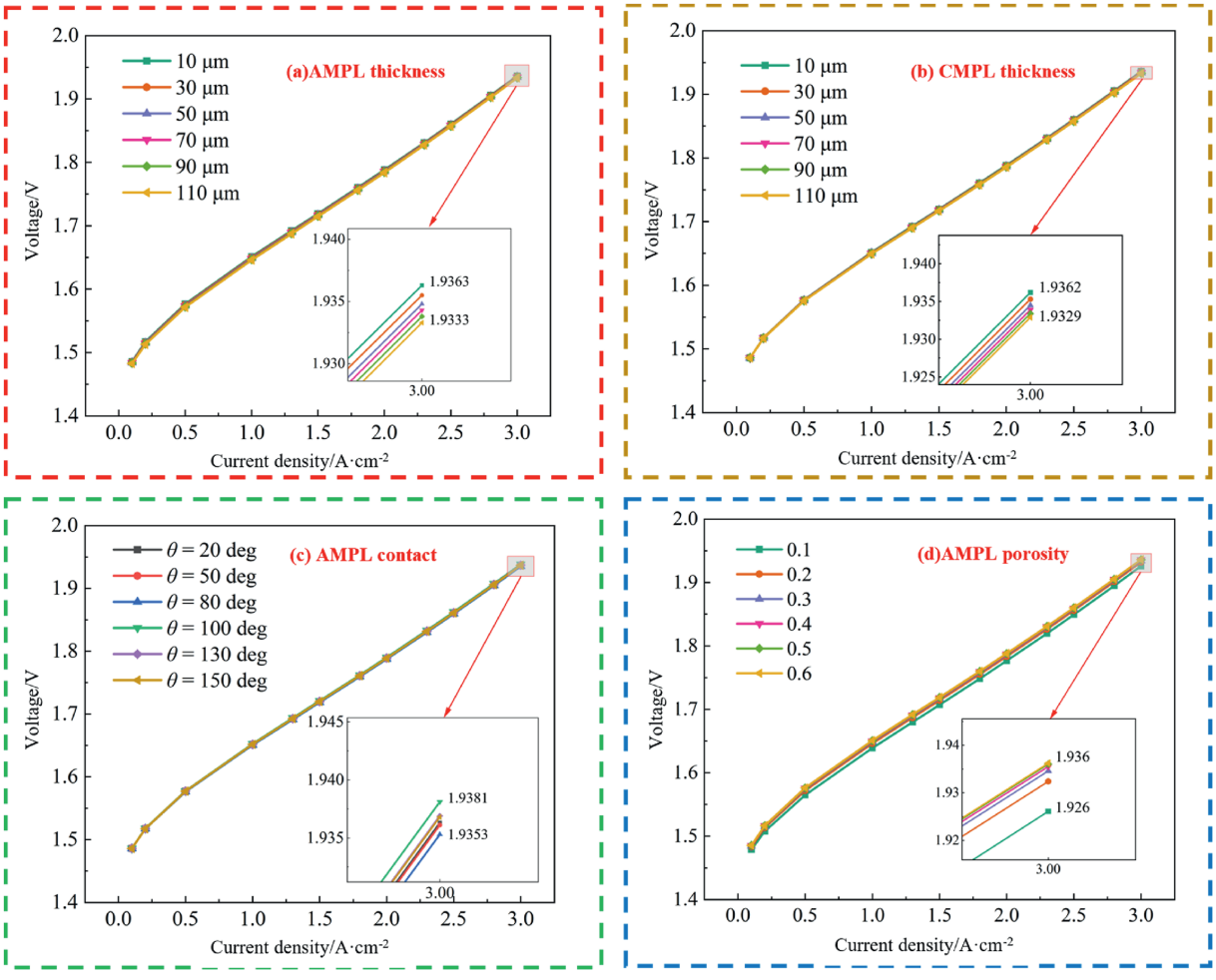


Fig. 8. Effect of AMPL(a) and CMPL(b) Thickness on electrolyzer performance, (c) Effect of cathode MPL contact angle on performance, (d) Effect of AMPL porosity on electrolyzer performance.

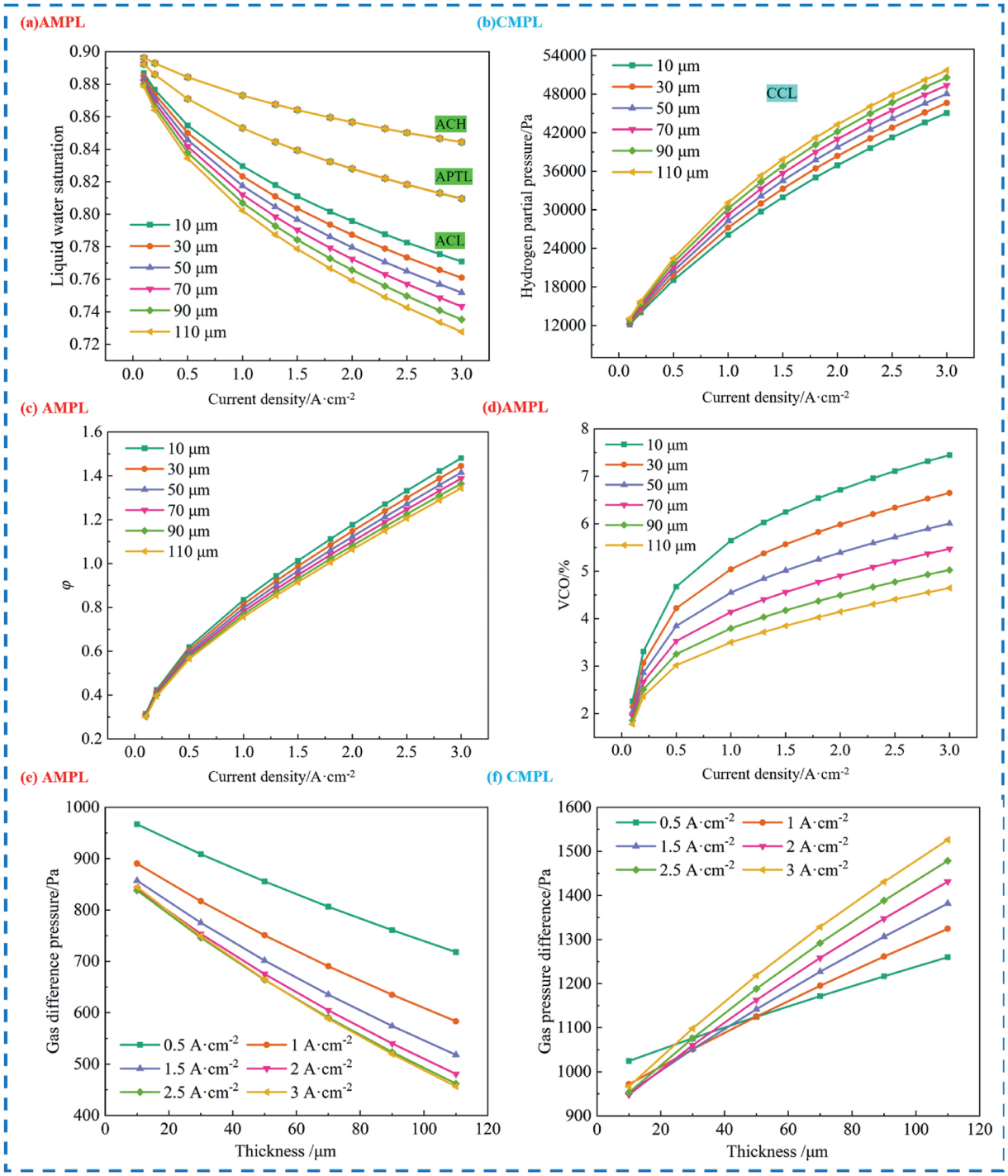


Fig. 9. (a) Effect of AMPL thickness on liquid water saturation, (b) Effect of CMPL thickness on the hydrogen partial pressure in CCL, (c) Effect of AMPL thickness on the Thiele modulus, (d) VCO with AMPL thickness at different current densities, Variation in transmembrane gas pressure difference with different AMPL(e) and CMPL(f) thicknesses.

in Fig. 9(d). Oxygen distribution uniformity decreases as the current density increases, whereas increasing AMPL thickness effectively enhances uniformity. At 3 A·cm^{-2}, increasing AMPL thickness from 10 to 110 μm reduces the VCO from 7.44% to 4.64%, corresponding to a 42.17% improvement. This improvement is attributed to variations in liquid water saturation across different regions of the CL, which influence water supply and bubble resistance, thereby affecting reaction uniformity. Typically, oxygen tends to accumulate near the outlet of the electrolyzer. The presence of an AMPL significantly enhances uniformity, particularly at greater thicknesses; however, diminishing returns are observed, as further increases yield progressively smaller improvements.

Fig. 9(e) and (f) shows the variation in transmembrane gas pressure difference with different AMPL and CMPL thicknesses. Increasing AMPL thickness raises the oxygen mole fraction in ACL and reduces the transmembrane gas pressure difference by up to 50%, thereby mitigating the adverse effects of hydrogen crossover. On the cathode side, the behavior differs. Except at 0.5 A·cm^{-2}, where the initial pressure difference is relatively higher than under other conditions, increasing CMPL thickness leads to a larger

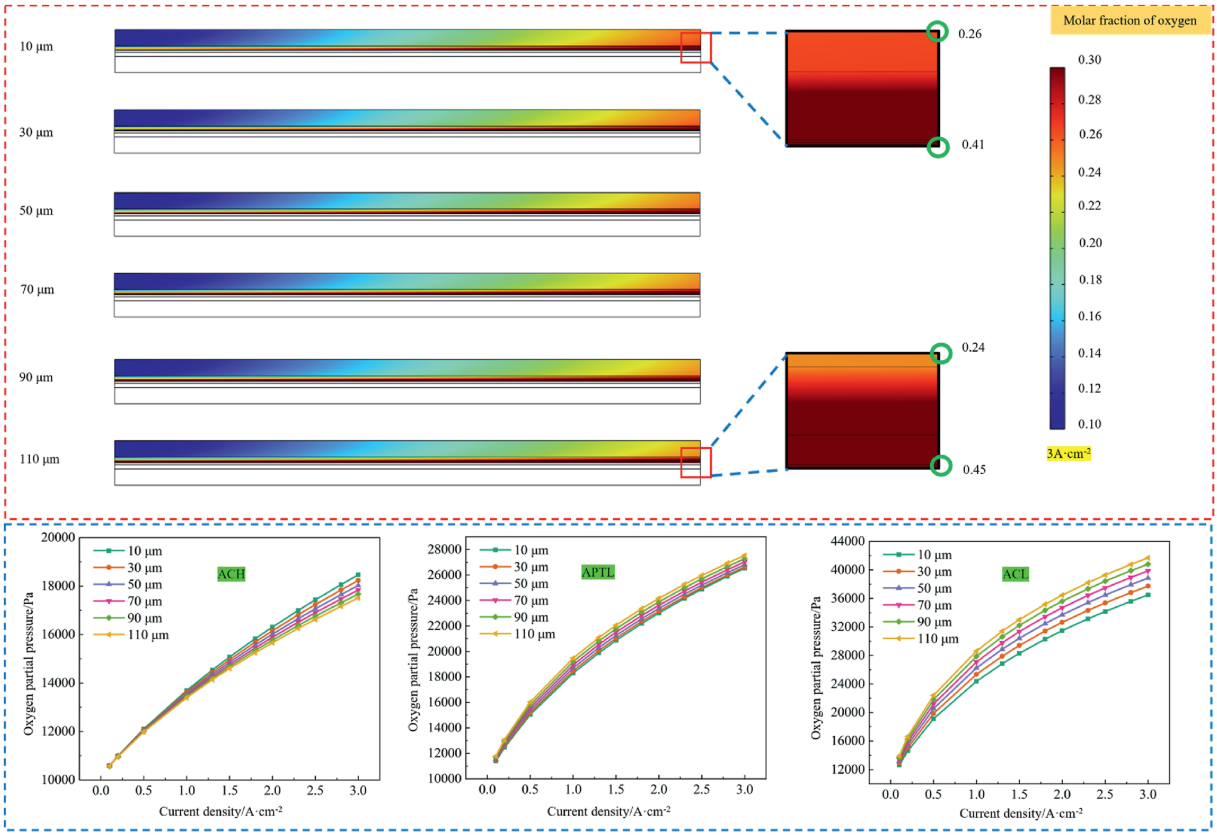


Fig. 10. Variations in oxygen mole fraction and partial pressure in the anode under different AMPL thicknesses.

transmembrane gas pressure difference. This effect becomes more pronounced with increasing current density, reaching a maximum of 960 Pa at 3 A·cm^{-2}. These results indicate that a thicker CMPL aggravates hydrogen accumulation in the CCL, thereby increasing the transmembrane gas pressure difference.

Fig. 10 illustrates the effect of AMPL thickness on the oxygen mole fraction and oxygen partial pressure in the anode. At 3 A·cm^{-2}, a thinner AMPL yields a higher oxygen mole fraction at the ACH outlet than a thicker one. The presence of an AMPL, especially at greater thickness, reduces the oxygen content in the ACH and promotes oxygen accumulation in the ACL. While a thicker AMPL retains more oxygen in the ACL, it simultaneously increases the diffusion resistance toward the channel.

In summary, analysis of the Thiele modulus and polarization curves indicates that although the addition of an AMPL, particularly with increased thickness, increases the oxygen mole fraction and causes oxygen accumulation in the ACL, it simultaneously enhances oxygen transport, improves electrolyzer performance, and enables operation at higher current densities. Therefore, the presence of an AMPL can partially reduce the hydrogen content in oxygen, thereby mitigating membrane degradation. With precise optimization, this effect can further enhance the durability and extend the lifetime of the membrane electrode.

3.4. Contact angle and porosity of the AMPL

AMPL contact angle of 80° yields the lowest liquid water saturation in the catalyst layer, As shown in Fig. 11(a), At 100°, the gas fraction in the ACL is minimized, as the AMPL drives more water into the layer and restricts gas transport. A hydrophilic MPL increases the oxygen mole fraction generated in the ACL. In contrast, a hydrophobic MPL accelerates oxygen transport toward the channel, increases the number of pores available for gas transfer, and thereby reduces oxygen transport resistance. By contrast, the CMPL contact angle has little effect on liquid water saturation.

Fig. 11(b) and (c) presents the influence of AMPL and CMPL contact angles on the transmembrane gas pressure difference. For the AMPL, the minimum pressure difference is observed at a contact angle of 80°, whereas the maximum occurs at 100°. In contrast, for the CMPL, the pressure difference reaches its maximum at 80° and its minimum at 100°. A more hydrophilic AMPL promotes water uptake, which reduces the number of pores available for gas transport, leading to oxygen accumulation in the ACL and elevated local pressure, thereby lowering the overall transmembrane gas pressure difference. The opposite behavior is observed under hydrophobic conditions. On the cathode side, increasing CMPL hydrophilicity lowers the transmembrane gas pressure difference, whereas greater hydrophobicity results in an increase. Specifically, higher hydrophilicity enhances liquid water saturation within the CMPL, suppressing hydrogen accumulation in the CCL, which decreases hydrogen content, reduces local pressure, and ultimately lowers the pressure difference. Conversely, increased hydrophobicity diminishes water retention in the CCL, facilitates gas accumulation, and elevates the hydrogen content, thereby increasing the pressure difference. Nevertheless, under comparable conditions, a more hydrophilic CMPL generally yields a higher transmembrane gas pressure difference than its hydrophobic counterpart.

The oxygen partial pressure distribution in the anode is shown in Fig. 11(d), (e) and (f). When the AMPL porosity is 0.1, the oxygen partial pressure in the ACL reaches its maximum. As the porosity increases, the oxygen partial pressure decreases, with the most

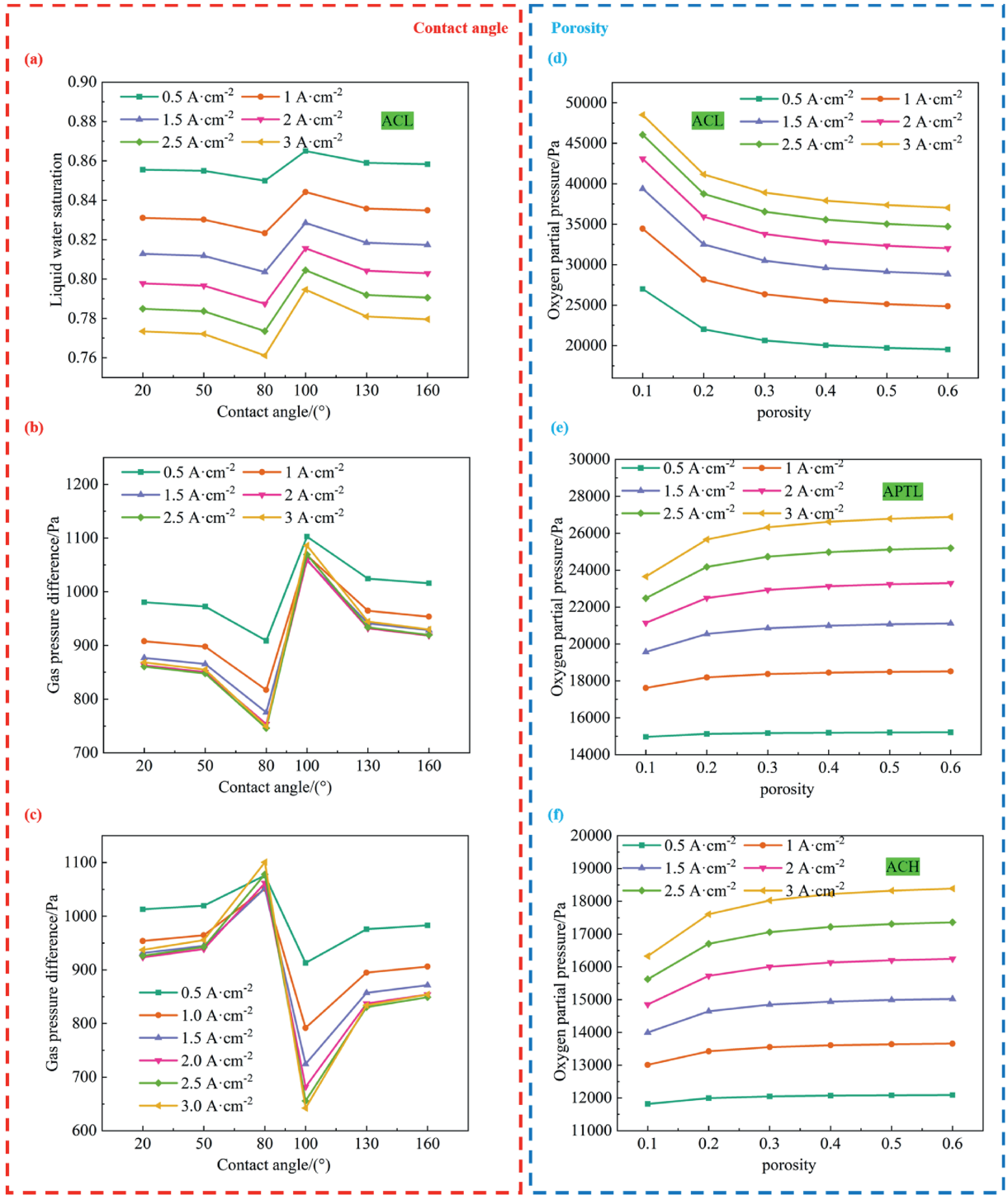


Fig. 11. (a) Variation of liquid water saturation in the ACL with different AMPL contact angles, Effect of AMPL(b) and CMPL(c) contact angles on the transmembrane gas pressure difference, oxygen partial pressure in ACL(d), APTL(e) and ACH(f) at different AMPL porosities.

pronounced reduction occurring between 0.1 and 0.2. Beyond this range (0.2–0.6), the rate of decline gradually diminishes. At low AMPL porosity, the oxygen partial pressures in the APTL and ACH remain relatively low; however, as porosity increases, these pressures rise progressively.

Fig. 12(a) and (b) illustrate the variation of the Thiele modulus (φ) under different porosities and the effect of AMPL porosity on oxygen distribution uniformity in the anode. At a given current density, increasing porosity gradually shifts the rate-limiting factor from reaction kinetics toward diffusion. The optimal operating condition is observed at 2 A·cm^{-2} with porosity≥0.3, where reaction and diffusion are relatively well balanced. At a porosity of 0.1, the oxygen distribution uniformity remains within 2% to 3%. With increasing porosity, uniformity improves, reaching 4% to 7% at 0.6. This trend can be attributed to the higher diffusion resistance of oxygen in low-porosity AMPLs, which suppresses rapid oxygen

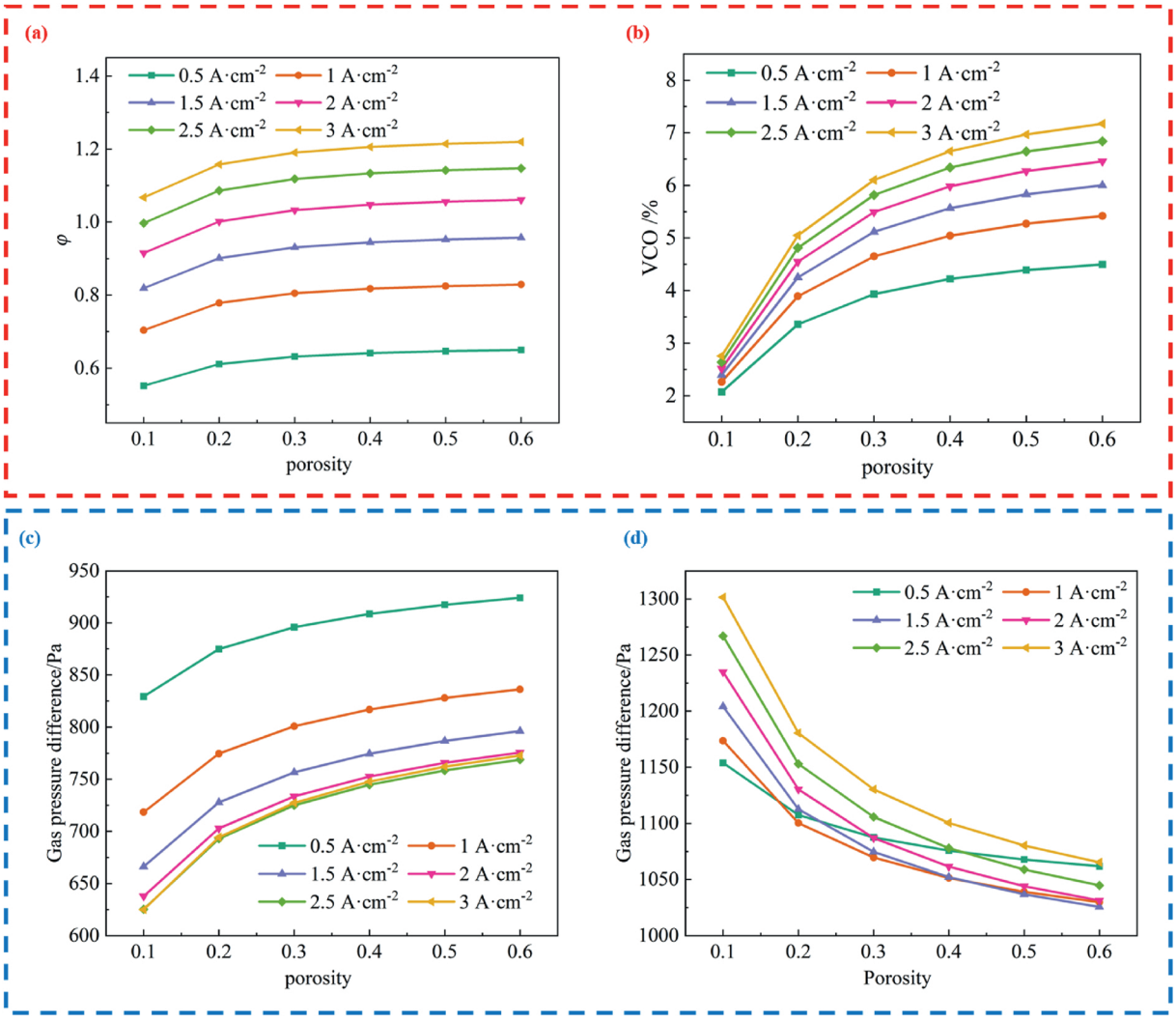


Fig. 12. (a) Thiele modulus as a function of AMPL porosity. (b) Effect of AMPL porosity on *VCO*, Effect of AMPL(c) and CMPL. (d) Porosity on the transmembrane gas pressure difference.

escape from local regions, promotes lateral redistribution, and mitigates concentration peaks. In addition, stronger capillary water-retention in low-porosity materials helps maintain liquid-water continuity at the CL/MPL interface, ensuring more stable oxygen transport and electrochemical reactions. Overall, both average gas retention and its spatial uniformity must be considered. Moderate reduction of AMPL porosity enhances oxygen distribution uniformity through multiple mechanisms, thereby supporting stable electrolyzer operation under high current densities. Accordingly, Fig. 12(c) and (d) illustrate the effect of porosity on the transmembrane gas pressure difference. As current density increases, the transmembrane gas pressure difference decreases because hydrogen escapes more readily than oxygen. When both hydrogen and oxygen production rates rise, the slower diffusion of oxygen leads to pressure buildup in the ACL, with the difference reaching up to 200 Pa between 0.5 and 3 $A \cdot cm^{-2}$. Moreover, increasing the AMPL porosity raises the transmembrane gas pressure difference by as much as 220 Pa, since higher porosity provides additional transport pathways and facilitates oxygen diffusion. The porosity of the cathode MPL also significantly influences the transmembrane gas pressure difference: greater porosity reduces hydrogen accumulation in the CCL, decreases diffusion resistance, increases diffusion pathways, and thereby lowers the pressure difference.

3.5. Best parameters of AMPL

Overall, as shown in Fig. 13, the MPL plays a pivotal role in regulating gas–liquid two-phase transport in PEMWEs by restructuring transport pathways between CL and PTL. The schematic illustration, together with the numerical results, indicates that MPL structural parameters must be carefully balanced to enhance oxygen transport while avoiding excessive mass-transfer resistance. Regarding thickness, an overly thin MPL provides insufficient regulation of oxygen removal and liquid-water distribution, whereas an excessively thick MPL introduces additional diffusion resistance and mass-transport losses. Within the investigated range, an intermediate-to-thick anode MPL (approximately 50–90 μm) offers the most favorable trade-off, simultaneously improving oxygen distribution uniformity, reducing liquid water saturation in the anode catalyst layer, and significantly lowering the transmembrane gas pressure difference.

Wettability exerts a similarly critical influence on transport behavior. Highly hydrophilic MPLs tend to flood pore spaces with liquid water, thereby impeding gas diffusion, while excessively hydrophobic MPLs weaken liquid-water continuity and promote local gas accumulation. The results demonstrate that a moderate contact angle of approximately 80° establishes an optimal balance between water retention and oxygen evacuation, leading to

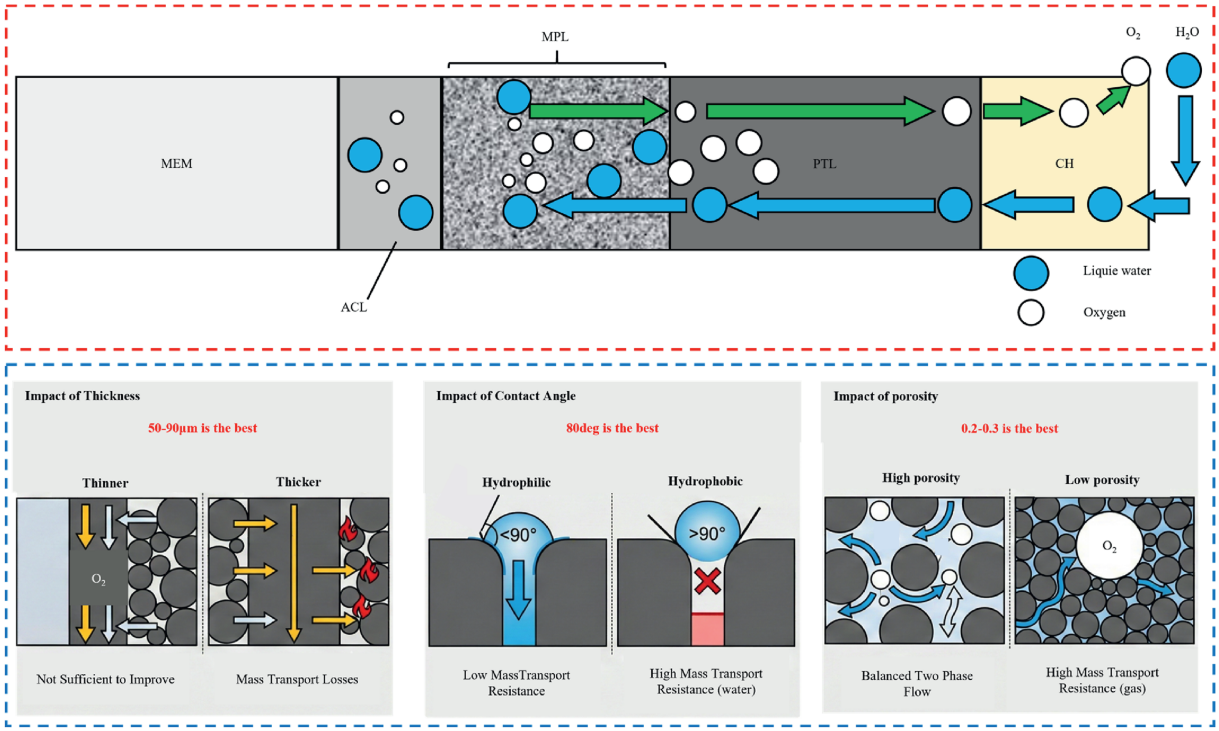


Fig. 13. The suggested AMPL parameters.

minimized mass-transfer resistance and a reduced transmembrane gas pressure difference.

Porosity further governs the competition between gas penetration and lateral redistribution. Although high porosity facilitates rapid gas transport, it favors the formation of preferential gas pathways and deteriorates oxygen distribution uniformity. In contrast, a moderately low porosity (approximately 0.2–0.3) enhances capillary forces and lateral diffusion, suppresses localized gas channeling, and promotes a more homogeneous two-phase flow. Collectively, these findings highlight that the coupled optimization of MPL thickness, wettability, and porosity is essential for achieving a balanced improvement in performance, transport uniformity, and operational safety at high current densities, with the anode MPL serving as the dominant structural element governing PEMWE mass transport and stability.

4. Conclusions

This study systematically elucidates the role of MPLs in PEM water electrolyzers using multiphysics numerical simulations. The results demonstrate that AMPL plays a dominant role in governing mass transport and operational stability, whereas CMPL exerts a comparatively weaker influence. The AMPL significantly reduces liquid water saturation in the anode catalyst layer, enhances oxygen mole fraction and distribution uniformity, and lowers the transmembrane gas pressure difference by up to 50%, thereby mitigating hydrogen crossover risk. In contrast, the CMPL provides only modest performance improvement but contributes to regulating local hydrogen accumulation and transmembrane gas pressure difference, which is relevant for safety-oriented design. The coupled effects of MPL structural parameters highlight the importance of balanced optimization. Increasing AMPL thickness improves oxygen transport, distribution uniformity, and pressure regulation, while excessive thickening introduces additional diffusion resistance. An intermediate-to-thick AMPL provides the most favorable trade-off. 50–90 μm is the best. Wettability exhibits a non-monotonic effect, with optimal contact angles of approximately 80° for the AMPL, reflecting a balance between water retention and gas evacuation. Increasing AMPL porosity degrades performance due to enhanced gas channeling and local accumulation, whereas a moderately low porosity (0.2–0.3) combined with sufficient thickness promotes lateral gas redistribution and stable operation at high current densities.

This study elucidates the coupled mechanisms by which electrode microstructures regulate two-phase transport, transmembrane gas pressure difference, and hydrogen crossover in PEMWE, with a systematic comparison of the respective roles of the AMPL and CMPL. The results demonstrate that the AMPL is the dominant structural factor governing anode mass transport and operational stability. Specifically, the AMPL effectively reduces the transmembrane gas pressure difference, thereby mitigating hydrogen crossover to the oxygen side, improving gas–liquid distribution, alleviating local oxygen supersaturation, and reducing stress concentration within the membrane–electrode assembly. Although the AMPL provides only limited direct improvement in voltage efficiency, it delays the onset of mass-transport limitations and contributes substantially to long-term durability and safe operation. In contrast, the CMPL plays a secondary but non-negligible role. While it can deliver a performance gain of several tens of millivolts, this benefit is accompanied by an increase in the transmembrane gas pressure difference, which may elevate the long-term risk of hydrogen crossover. When both MPLs are employed, the transmembrane gas pressure difference tends to increase at high current densities, indicating that improper CMPL design can partially offset the safety benefits introduced by the AMPL. Consequently, the CMPL should be regarded primarily as an auxiliary tuning element for performance enhancement, whose parameters must be carefully constrained to avoid adverse impacts on safety. For configurations incorporating both MPLs, coordinated optimization of thickness, porosity, and

wettability is essential to balance performance gains against pressure-driven crossover risks.

It should be noted that the present two-dimensional model assumes uniform in-plane distributions of reactant concentration and current density, thereby neglecting the local obstruction effects induced by rib/channel structures. As a result, gas transport pathways, gas retention, and local pressure losses beneath the ribs are not fully captured, and local mass-transport resistance is likely underestimated due to tortuosity effects. In practical electrolyzers, pronounced in-plane gradients of concentration and current density exist; regions beneath the ribs experience longer transport paths and higher resistance, making them more susceptible to local mass-transport limitations, gas accumulation, and amplified transmembrane pressure differences. Furthermore, the tortuous flow paths inherent to realistic three-dimensional structures increase effective transport distances, intensify local pressure losses, and exacerbate non-uniformities in concentration and current distribution. Consequently, the uniformity and durability predicted by the two-dimensional model are, to some extent, overestimated relative to real devices. Future work should therefore focus on developing more realistic three-dimensional, fully coupled multiphysics models to improve predictive capability and to more accurately evaluate electrolyzer uniformity, safety, and durability. In parallel, advanced composite optimization strategies—such as gradient pore-size distributions and gradient hydrophilic–hydrophobic architectures—merit investigation to achieve synergistic gas–liquid transport regulation and structural robustness, thereby supporting the efficient, safe, and scalable deployment of PEM water electrolyzers.

CRediT Authorship Contribution Statement

Lei Zhang: Writing – review & editing, Writing – original draft. Youliang Cheng: Methodology. Yipeng Zhang: Resources, Data curation. Chen Ju: Visualization. Tianrang Yang: Funding acquisition.

Author Declaration

We confirm that the manuscript has been read and approved by all named authors and that there are no other persons who satisfied the criteria for authorship but are not listed. We further confirm that the order of authors listed in the manuscript has been approved by all of us.

We confirm that we have given due consideration to the protection of intellectual property associated with this work and that there are no impediments to publication, including the timing of publication, with respect to intellectual property. In so doing we confirm that we have followed the regulations of our institutions concerning intellectual property.

We understand that the Corresponding Author is the sole contact for the Editorial process (including Editorial Manager and direct communications with the office). He is responsible for communicating with the other authors about progress, submissions of revisions and final approval of proofs. We confirm that we have provided a current, correct email address which is accessible by the Corresponding Author and which has been configured to accept email from.

Acknowledgements

This work was supported by the National Key Research and Development Program of China (2023YFB4005000).

References

[1] S. Sakaida, S. Nakamura, H. Makino, K. Tanaka, Enhancing high-current-density performance of polymer electrolyte fuel cells using ultra-thin GDL/MPLs, *J. Power Sources* 655 (2025) 237937.
[2] H. Zhang, H. Hu, M. Sarker, X.Y. Shao, Z.G. Zhan, P.C. Sui, P.A. Chuang, Numerical investigation of effect of mechanical compression on the transport properties of fuel cell microporous layer using a pore-scale model, *Int. J. Hydrogen Energy* 62 (2024) 591–600.
[3] H. Zhang, L.J. Zhu, M. Sarker, M.L. Wang, H. Chang, D.L. Kui, Z.G. Zhan, Pore-scale simulations investigating mechanical compression effects on transport properties at gas diffusion layer/micro-porous layer interfaces in proton exchange membrane fuel cells, *J. Power Sources* 642 (2025) 236962.
[4] Z. Tayarani-Yoosefabadi, J. Bellerive, E. Kjeang, Multiscale stochastic modeling of microporous layers and bi-layer gas diffusion media for polymer electrolyte fuel cells, *J. Power Sources* 581 (2023) 233476.
[5] A. Nishimura, K. Yamamoto, T. Okado, Y. Kojima, M. Hirota, M.L. Kolhe, Impact analysis of MPL and PEM thickness on temperature distribution within PEFC operating at relatively higher temperature, *Energy* 205 (2020) 117875.
[6] A. Nishimura, T. Okado, Y. Kojima, M. Hirota, E. Hu, Impact of MPL on temperature distribution in single polymer electrolyte fuel cell with various thicknesses of polymer electrolyte membrane, *Energies* 13 (10) (2020) 2499.
[7] P.A. García-Salaberri, A. Sánchez-Ramos, A numerical analysis of the effect of layer-scale and microscopic parameters of membrane electrode assembly in proton exchange fuel cells under two-phase conditions, *J. Power Sources* 593 (2024) 233950.
[8] Y.C. Chen, C. Karageorgiou, J. Eller, T.J. Schmidt, F.N. Büchi, Determination of the porosity and its heterogeneity of fuel cell microporous layers by X-ray tomographic microscopy, *J. Power Sources* 539 (2022) 231612.
[9] S.B. Lan, R. Lin, M.C. Dong, K. Lu, M.Y. Lou, Image recognition of cracks and the effect in the microporous layer of proton exchange membrane fuel cells on performance, *Energy* 266 (2023) 126340.
[10] T. Jiang, C.L. Han, X. Wang, Q. Ma, Y.X. Zhu, Z.Q. Chen, Optimization of microporous layer perforation design for enhanced liquid water management in PEM fuel cells, *Int. J. Heat Mass Tran.* 236 (2025) 126277.
[11] N.R. Wu, D.D. Hou, Q. Zhang, Y. Liu, A.Y. Yao, J. Yang, S.P. Zhang, R.Y. Song, D. X. Zhang, Y. Qi, R.Z. Yang, L.D. Wang, Precisely engineered microporous layers for proton exchange membrane fuel cells with high power density, *ACS Sustainable Chem. Eng.* 11 (17) (2023) 6545–6555.
[12] H.Y. Song, Y.T. Liu, W.S. Zhang, X.F. Zhang, X. Yin, J.F. Li, G.P. Wu, Rational design of carbon network structure in microporous layer toward enhanced mass transport of proton exchange membrane fuel cell, *J. Power Sources* 539 (2022) 231623.
[13] S. Liu, T. Ma, H.K. Jia, Q.S. Zhang, G.J. Xu, Study of the effect of pore properties of microporous layer on water transport process in proton exchange membrane fuel cell, *Int. Commun. Heat Mass Tran.* 159 (2024) 108198.
[14] A. Mohseninia, D. Kartouzian, M. Eppler, P. Langner, H. Markötter, F. Wilhelm, J. Scholta, I. Manke, Influence of structural modification of micro-porous layer and catalyst layer on performance and water management of PEM fuel cells: hydrophobicity and porosity, *Fuel Cells* 20 (4) (2020) 469–476.
[15] X. Li, R.L. Liu, M. Yao, J.B. Zhang, Y. Liu, Performance of polymer electrolyte fuel cell under wet/dry conditions with hydrophilic and hydrophobic electrospun microporous layers, *J. Power Sources* 545 (2022) 231896.
[16] G.Y. Lin, S.Y. Liu, S.Y. Qu, G.K. Qu, T.Y. Li, Z.N. Liang, Y.F. Hu, F.M. Liu, Effects of thickness and hydrophobicity of double microporous layer on the performance in proton exchange membrane fuel cells, *J. Appl. Polym. Sci.* 138 (18) (2021) 50355.
[17] R. Lin, D. Zhong, S.B. Lan, R. Guo, Y.Y. Ma, X. Cai, Experimental validation for enhancement of PEMFC cold start performance: based on the optimization of micro porous layer, *Appl. Energy* 300 (2021) 117306.
[18] Q. Zhang, T.Y. Gu, R.H. Shi, J. Yan, W. Wang, W. Qian, B.W. Zhai, M.Z. Zhou, M. R. Chai, R.Z. Yang, Silane-functionalized carbon with super-hydrophobicity advancing microporous layer for proton exchange membrane fuel cells, *J. Power Sources* 555 (2023) 232342.
[19] P. Wang, H. Nakajima, T. Kitahara, Hydrophilic and hydrophobic composite microporous layer coated gas diffusion layers for performance enhancement of polymer electrolyte fuel cells, *J. Electrochem. Soc.* 171 (1) (2024) 014501.
[20] Y. Ira, Y. Bakhshan, J. Khorshidimalahmadi, Effect of adding simultaneous hydrophilic and microporous layers on water transport in the gas diffusion layer of polymer electrolyte membrane fuel cell, *Proc. Inst. Mech. Eng. Part A J. Power Energy* 236 (1) (2022) 61–80.
[21] N.R. Wu, Y. Liu, X.X. Tian, F.Y. Liu, Y.C. Ma, S.P. Zhang, Q. Zhang, D.D. Hou, Y. Qi, R.Z. Yang, L.D. Wang, The microporous layer in proton exchange membrane fuel cells, from transport mechanism to structural design, *J. Power Sources* 580 (2023) 233412.
[22] J.N. Yang, X.Y. Wang, Z.Y. Ding, Z.Y. Kang, B. Wang, Z.T. Du, M. Wang, F.Y. Zhang, Combining materials development with structural design: insights into porous transport layer for proton exchange membrane water electrolysis, *Renew. Sustain. Energy Rev.* 223 (2025) 116030.
[23] L. Ding, Z.Q. Xie, W.T. Wang, F.Y. Zhang, Enhancing reaction interface with modified microporous layers for high-efficiency hydrogen production in PEM water electrolysis, *Electrochim. Acta* 502 (2024) 144757.
[24] J.J. Wang, D.D. Ye, J. Huang, Q. Peng, F. Chen, B. Mecheri, A. D'Epifanio, E. Traversa, J. Song, G.Z. Xu, J. Li, X. Zhu, Q. Liao, Dual functionality of cathode microporous layers: reducing hydrogen permeation and enhancing

performance in proton exchange membrane water electrolyzers, *Chem. Eng. J.* 500 (2024) 157060.
[25] M.F. Ernst, V. Meier, M. Kornherr, H.A. Gasteiger, Preparation and performance evaluation of microporous transport layers for proton exchange membrane (PEM) water electrolyzer anodes, *J. Electrochem. Soc.* 171 (7) (2024) 074511.
[26] J.X. Zou, Y.B. Sun, X.Y. Wang, J.T. Chen, J.K. Mo, S.G. Wu, Q.R. Chen, C.K. Zhao, H.J. Wang, M. Wang, Hierarchical porous transport layers for enhancing mass transport in proton exchange membrane electrolyzer cells, *eTransportation* 26 (2025) 100510.
[27] T. Schuler, C.C. Weber, J.A. Wrubel, L. Gubler, B. Pivovar, F.N. Büchi, G. Bender, Ultrathin microporous transport layers: implications for low catalyst loadings, thin membranes, and high current density operation for proton exchange membrane electrolysis, *Adv. Energy Mater.* 14 (7) (2024) 2302786.
[28] J.X. Zou, Z.Y. Zhu, Y.B. Sun, K.G. Yao, Z.N. Li, M. Wang, H.J. Wang, Wettability-gradient gas diffusion layers: enhancing water management in electrochemical hydrogen compressors, *ACS Sustainable Chem. Eng.* 13 (33) (2025) 13414−13426.
[29] K.G. Yao, Z.Y. Zhu, Y.B. Sun, J.X. Zou, M. Wang, H.J. Wang, Enhanced low-humidity performance of electrochemical hydrogen compressors through efficient water management with Janus gas diffusion layers, *Int. J. Hydrogen Energy* 150 (2025) 150129.
[30] D. Kulkarni, R. Ouimet, B. Erb, D.Y. Parkinson, H.M. Chang, C. Wang, A. Smeltz, C. Capuano, I.V. Zenyuk, Influence of microporous layers on interfacial properties, oxygen flow distribution, and durability of proton exchange membrane water electrolyzers, *ACS Appl. Mater. Interfaces* 15 (41) (2023) 48060−48071.
[31] Q.H. Zeng, X.H. Yang, H.L. Xu, Z.T. Liu, X.Y. Gao, Numerical simulation of comprehensive performance of proton exchange membrane electrolytic cell with microporous layer, *Int. J. Hydrogen Energy* 77 (2024) 495−510.
[32] A.D. Tan, F. Zhao, Y.P. Zhang, G. Li, C. Wu, Z. Liu, J. Li, J.G. Liu, Innovative application of transfer learning on small-scale datasets: analysis and optimization of catalyst ink for the low-iridium membrane electrode assemblies of proton exchange membrane water electrolysis, *Chem. Eng. Sci.* 302 (2025) 120814.
[33] M.Y. Xu, J.D. Li, Y.Z. Qin, Y.J. Wang, X.H. Du, G.H. Liu, Numerical study of proton exchange membrane water electrolyzer performance based on catalyst layer agglomerate model, *Chem. Eng. J.* 499 (2024) 156371.
[34] J. Yao, Z. Wu, H. Wang, F.S. Yang, J. Xuan, L. Xing, J.W. Ren, Z.X. Zhang, Design and multi-objective optimization of low-temperature proton exchange membrane fuel cells with efficient water recovery and high electrochemical performance, *Appl. Energy* 324 (2022) 119667.
[35] B.S. Machado, M. Mamlouk, N. Chakraborty, Three-dimensional agglomerate model of an anion exchange membrane fuel cell using air at the cathode—A parametric study, *J. Power Sources* 412 (2019) 105−117.
[36] X. Ma, X.Q. Zhang, J.P. Yang, W.L. Zhuge, S.J. Shuai, Impact of gas diffusion layer spatial variation properties on water management and performance of PEM fuel cells, *Energy Convers. Manag.* 227 (2021) 113579.
[37] H. Chen, H. Guo, F. Ye, C.F. Ma, Modification of the two-fluid model and experimental study of proton exchange membrane fuel cells with baffled flow channels, *Energy Convers. Manag.* 195 (2019) 972−988.
[38] R.J. Fan, G.F. Chang, Y.M. Xu, J.M. Xu, Multi-objective optimization of graded catalyst layer to improve performance and current density uniformity of a PEMFC, *Energy* 262 (2023) 125580.
[39] B.S. Machado, M. Mamlouk, N. Chakraborty, Entropy generation analysis based on a three-dimensional agglomerate model of an anion exchange membrane fuel cell, *Energy* 193 (2020) 116667.
[40] X.K. Yang, Q.X. Xiang, D.H. Fang, S.C. Sun, J.K. Hao, F. Xie, Z.G. Shao, Simulation and experimental investigation of a novel chain-shaped flow field for proton exchange membrane fuel cell, *Energy Convers. Manag.* 315 (2024) 118797.
[41] G.B. Zhang, K. Jiao, Three-dimensional multi-phase simulation of PEMFC at high current density utilizing Eulerian-Eulerian model and two-fluid model, *Energy Convers. Manag.* 176 (2018) 409−421.
[42] L. Xing, W.D. Shi, H.N. Su, Q. Xu, P.K. Das, B.D. Mao, K. Scott, Membrane electrode assemblies for PEM fuel cells: a review of functional graded design and optimization, *Energy* 177 (2019) 445−464.
[43] S.N. Liu, J.Q. Tan, H.Q. Hu, C.L. Lu, D.J. Xuan, Multi-objective optimization of proton exchange membrane fuel cell geometry and operating parameters based on three new performance evaluation indexes, *Energy Convers. Manag.* 277 (2023) 116642.
[44] L. Xing, M. Mamlouk, R. Kumar, K. Scott, Numerical investigation of the optimal Nafion® ionomer content in cathode catalyst layer: an agglomerate two-phase flow modelling, *Int. J. Hydrogen Energy* 39 (17) (2014) 9087−9104.
[45] B. Xie, G.B. Zhang, J. Xuan, K. Jiao, Three-dimensional multi-phase model of PEM fuel cell coupled with improved agglomerate sub-model of catalyst layer, *Energy Convers. Manag.* 199 (2019) 112051.
[46] Y.L. Wang, T. Liu, H. Sun, W. He, Y.Z. Fan, S.X. Wang, Investigation of dry ionomer volume fraction in cathode catalyst layer under different relative humilities and nonuniform ionomer-gradient distributions for PEM fuel cells, *Electrochim. Acta* 353 (2020) 136491.